TAMPEREEN TEKNILLINEN YLIOPISTO
TAMPERE UNIVERSITY OF TECHNOLOGY

HOANG NGUYEN

NANOPARTICLES-CONTAINING GLASSES USING DIRECT DOPING METHOD

Master of Science Thesis

Examiner(s):
Assist. Prof. Laeticia Petit
Mikko Hokka
Examiner and topic approved on 29.11.2017

ABSTRACT

HOANG NGUYEN: Nanoparticles-containing glasses using direct doping method
Tampere University of technology
Master of Science Thesis, 65 pages, 0 Appendix page(s)
November 2017
Master's Degree Programme in Materials Technology
Major: Metals and Ceramics
Examiner: Professor Laeticia Petit

Keywords: upconversion, nanoparticles, direct doping

In this thesis, the direct doping method was optimized to prepare microparticles $CaAl_2O_4$: Eu^{2+}, Nd^{3+} and nanoparticles $NaYF_4$: Yb^{3+}, Er^{3+} containing oxyfluoride phosphate glasses. The produced samples were characterized using SEM/EDS, FTIR and Raman spectroscopies, photoluminescence or upconversion measurement. In this work, new oxyfluoride glasses were processed within the system $90NaPO_3$-$(10-x)Na_2O$-$xNaF$ with x ranging from 0 to 10 (in mol%) and characterized. The progressive replacement of Na_2O by NaF increases the network connectivity. Their melting temperature is lower than 750°C and well-suited for adding active $NaYF_4$ nanoparticles. The direct doping method was applied successfully to produce upconverter oxyfluoride glasses. The best doping parameters here were identified: 575°C as the doping temperature and 3-minute dwell time, which most effectively balance the dispersion and survival of the particles in the glass. However, these parameters can still be adjusted for even better results. In addition, we showed that the corrosive behavior between the host and the particles depends not only on the glass melting temperature, but also on the nature of the particles.

PREFACE

The thesis work was carried out under the International Master Degree program of Materials Science department at Tampere University of Technology (TUT), Finland. The experimental part was conducted in the Laboratory of Photonics, in the group of Photonic Glasses led by Assistant Professor Laeticia Petit. The analysis part was supported by collaborations from Dr. Mika Lastusaari from University of Turku (UTU) and internal corporation with Dr. Turkka Salminen.

Having achieved this interesting thesis, I am sincerely grateful to Dr. Petit for her support throughout the period. Additionally, I would like to thank other lab-mates for excellent cooperation, and to the great collaborations with Dr. Lastusaari as well as Dr. Salminen.

Tampere, 22.11.2017

HOANG NGUYEN

CONTENTS

LIST OF FIGURES

LIST OF TABLES

LIST OF SYMBOLS AND ABBREVIATIONS

$(NaPO_3)_6$	sodium(I) hexametaphosphate
ΔG_v	crystal-glass free energy difference
Δm	change in mass
°C	degrees Celsius (0 °C = 273.15K)
µm	micrometer (1 µm = 10^{-6} m)
A	absorbance
a.u.	arbitrary unit
Al_2O_3	aluminum(III) oxide
ATR	Attenuated Total Reflection
b	non-zero positive integer
BBV	beam-bending viscometer
$CaAl_2O_4:Eu^{2+},Nd^{3+}$	bivalent europium and trivalent dysprosium doped calcium (II) aluminum(III) oxide
CCDs	charge-coupled devices
cm	centimeter (1 cm = 10^{-2} m)
DSC	Differential Scanning Calorimetry
EDS	energy dispersive X-ray spectrometry
EDS	Energy-dispersive X-ray Spectroscopy
Er^{3+}	trivalent erbium ion
ESA	excited-state absorption
ETU	energy transfer upconversion
FTIR	Fourier Transform Infrared Spectroscopy
g	gram (1 g = 10^{-3} kg)
I	nucleation rate kinetics
I_0	rate of steady state nucleation
IR	infrared
$LiYF_4$	lithium yttrium fluoride
$LiYF_4$	yttrium lithium fluoride
Ln^{3+}	trivalent lanthanum ion
m	mass
M	molar mass
ml	milliliter (1 ml = 1 cm^3)
mm	millimeter (1 mm = 10^{-3} m)
MP(s)	microparticle(s)
MPs	microparticles
MR	multiphonon relaxation
n	molar amount
Na_2O	sodium(I) oxide
$NaPO_3$	sodium(I) metaphosphate
$NaYF_4$	sodium yttrium fluoride
NIR	near-infrared
nm	nanometer (1 nm = 10^{-9} m)
NP(s)	nanoparticle(s)
NPs	nanoparticles
P_2O_5	phosphorus(V) oxide
PeL	Persistent luminescence
PL	conventional luminescence
PMT	photomultiplier tubes

PPV	parallel-plate viscometer
RE	rare earth
SEM	scanning electron microscope
SiO_4^{4-}	orthosilicate ion
t	time
T_f	fictive temperature
T_g	glass transition temperature
T_p	peak of crystallization temperature
TUT	Tampere University of Technology
T_x	onset of crystallization temperature
UC	upconversion
UV	ultraviolet
UV-Vis-NIR	ultraviolet-visible-near infrared
x	fraction of component
XRD	X-ray powder diffraction
YAG	yttrium aluminium garnet
YF_3	yttrium(III) fluoride
α	absorption coefficient
ΔG	free-energy change per unit volume corresponding to the new phase formation
ΔG_E	elastic distortion energy
θ	contact angle
λ	wavelength
ρ	density

1. INTRODUCTION

The invention of lasers in 1960s was a milestone in human history and marked the birth of photonic science. Nowadays, photonic researches cover the light generation, transmission, modulation, amplification, conversion or detection in which glasses are the number 1 material due to their outstanding optical properties [Pa, 14.]. Among those, laser glasses have attracted great interest. They can amplify light due to the rare-earth (RE) ions. Such laser glasses have found applications in almost every crucial technology fields of the modern world. [Ya, 00.]

The performance of laser glasses can be significantly improved if the RE ions are incorporated in crystals rather than in amorphous glass network. This leads to the application of glass-ceramic. Such materials can be obtained by heat treating a glass to grow in-situ crystals. However, the main difficulty is to control the growth of RE doped crystals in the bulk [Ca, 14]. Fortunately, recent discovery with the direct doping method from Zhao et al [Zh, 16] has given detailed information to successfully fabricate nanoparticles-containing telluride-based glasses. The technique utilizes pre-processed, chemically synthesized nanoparticles doped with RE elements which are directly integrated into the glass after melting. As the method is very promising, this thesis aims at applying it for another popular glass system—oxyfluoride phosphate glasses.

The first experimental part was to optimize the direct doping method in oxyfluoride phosphate glasses for uniformly dispersing the particles while preserving their spectroscopic properties in the glass. At the beginning, persistent luminescent microparticles were used as they are much easier to analyze than nanoparticles due to their size and due to their afterglow properties. Then, nanoparticles containing glasses were prepared using the optimized direct doping method. The study's results are thoroughly interesting and provide valuable information for further researches in the future.

After the introduction, the thesis continues to Chapter 2 presenting basic knowledge about laser glasses, doping methods and the upconversion nanoparticles. Chapter 3 provides practical details about the materials (particles and host glass composition), characterization methods (SEM, density, viscosity, DSC, IR/Raman, luminescence) including their theory. The study's results and discussion are followed in Chapter 4. Finally, interesting observations are concluded in the final chapter.

2. RESEARCH BACKGROUND

2.1 Glasses

2.1.1 Glass definition

Glass is praised as “a mysterious material” by Professor Eric Le Bourhis in his book “Glass: Mechanics and Technology”, not due to its long-lasting misconception of the “fourth state of matter”, but because its properties are massively changed by the way it is produced. The most common definition states this material is “an amorphous solid showing a glass transition”. In other words, glass is created when quenching a liquid it passes the melting/liquidus temperature, “frozen” structure happens, not crystallization because the end temperature is too low for the atoms to rearrange in long-range order. [Le, 07.] The schematic diagram of glass formation mechanism is displayed in Figure 1.

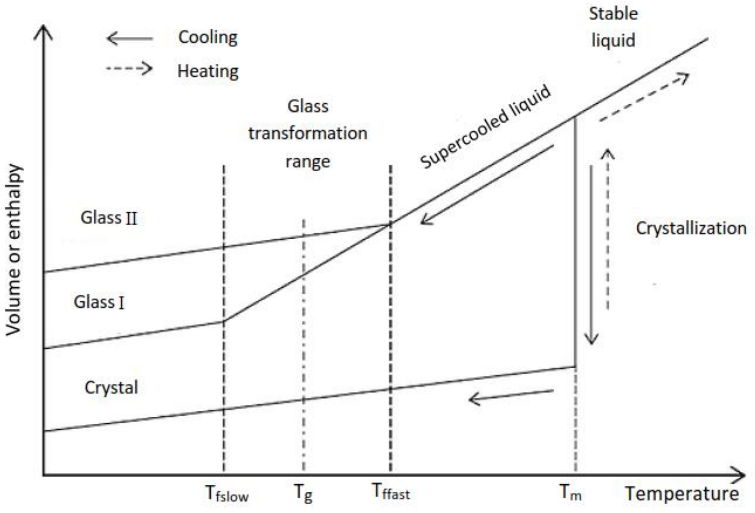

Figure 1. Glass formation mechanism diagram [Fa, 03].

On one hand, when a liquid is cooled down slowly enough from its stable state to under the melting point, crystals are formed with a significant decrease in volume or enthalpy. The nucleation and growth rates are determined by the viscosity as well as the crystal–glass free energy difference (ΔG_v). On the other hand, when the cooling rate is fast enough to bypass the melting point, the liquid becomes supercooled; further reduction in temperature can lead to two types of glasses depending on the cooling speed at this stage. It should be noted that the volume/enthalpy does not decrease as suddenly as in crystallization. As depicted in the Figure 1, the two glass lines intersect with the supercooled (extrapolated) line at the T_f— the fictive temperature, where T_{fslow} and T_{ffast} denote the fictive points corresponding to the slow and fast cooling rate in the glass formation part.

In other words, T_f represents the glass thermal history. The fictive temperature is important not only because it affects many properties but also it determines the glass transition temperature (T_g), clarifying the onset temperature of glass transformation. [Ya, 00.]

After cooling, the resulting crystalline or glass solid have different structure. The former possesses a long-range, well-defined order (Figure 2a, taken as an example), thus having a precise melting point. This structure is also so typical that it produces a distinctive X-ray diffraction pattern for realizing a specific crystalline material. On the contrary, the glass structure has random, short-range order as well as irregular interatomic distances and coordination number as seen in Figure 2b which pictures the network of SiO_2 glass. As a result, a glass solid provides neither specific X-ray patterns nor fixed melting temperature. As shown in Figure 2c, it is possible to modify the glass structure by adding other elements such as Na_2O in SiO_2 glass. In this example, the addition of Na_2O creates non-bridging oxygens at the expense of bridging oxygens.

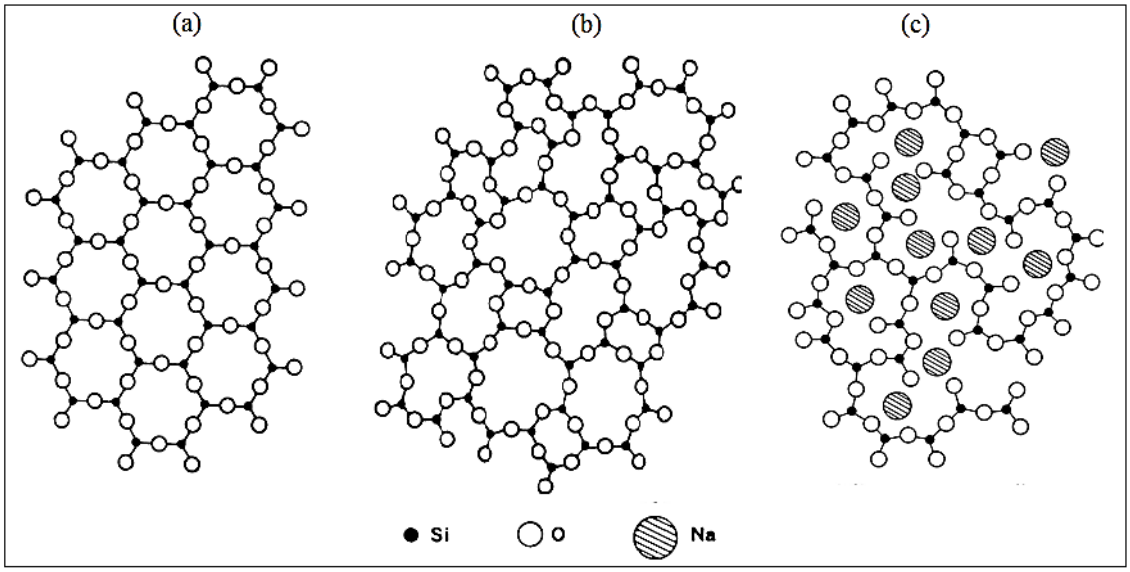

Figure 2. Silicon dioxide's a) crystal structure; b) glass structure and c) glass structure with Sodium network modifier [Ya, 00].

2.1.2 Glass systems

Silicate glasses are probably the most common system. Their glass structure composes of silica and surrounding modifier elements for the sake of manufacturing. The silicate glasses' network is made from corner-linked [SiO_4^{4-}] tetrahedral units in which silicon locates in the center (Figure 3a). In practice, all corners are linked in the same fashion with each oxygen is shared between 2 silicons [Sh, 05]. The silica 3D-network is dense and tight, thus limiting the solubility of RE ions. [Ya, 00].

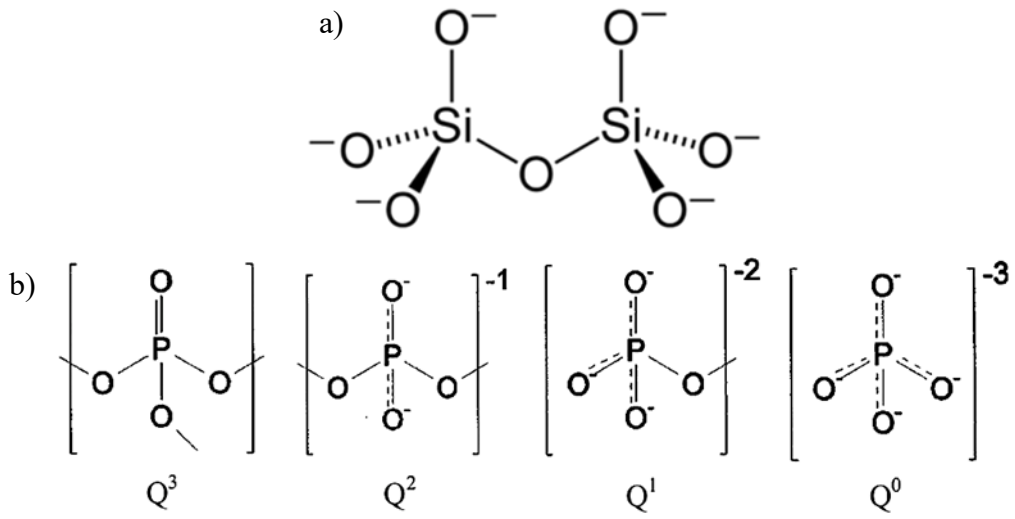

Figure 3. Simplified illustration of a) silica and b) phosphate units [Ib, 12].

On the contrary, phosphate glasses are easy to process (lower melting point than silicate glasses). They are also thermally stable and suitable for the applications with high transparency in the Ultraviolet-Visible-Near Infrared (UV-Vis-NIR) region [Ji, 97], [Ca, 00], [Ga, 82], [Ji, 98], [Pu, 16]. The structure of phosphate glasses contains long chains of phosphate units linked by oxygen atoms. The number of bridging oxygens (n) per unit indicates a specific structural Q^n unit. Different Q-units in phosphate networks are depicted in Figure 3b.

2.1.3 Laser glasses

The first man-made glass has been found in tombs in Egypt dating back to 3500 BC. Since then, the glass transparency became more and more importance. The chapter of optical glasses begins in 17th century with the first appearance of flint glasses (vases, goblets etc.) as well as advanced optics in microscopic/astronomic instruments [Le, 07]. Overtime, glasses have been used widely, from daily (glazing, packaging…) to super hi-tech products. In modern science, there are two branches of optical glasses: Optoelectronics and Photonics. Laser glasses belong to the latter. [Ga, 06.]

Laser glasses are glasses doped with rare-earth (RE) elements. These are 17 chemical elements in the periodic table (Figure 4 including 15 lanthanides (lanthanum to lutetium), plus scandium and yttrium). The rare-earth ions are widely utilized in research because their electron structure provides various options from multiple usable fluorescing states and wavelengths, enabling a diverse range of applications [Ya, 00]. In addition, doping RE ions in glasses is the only way to achieve laser emission because of the larger line broadening of phonon spectra and optical emission in glass than in crystal (a result from the glass's randomly structural order) [Ga, 06.]

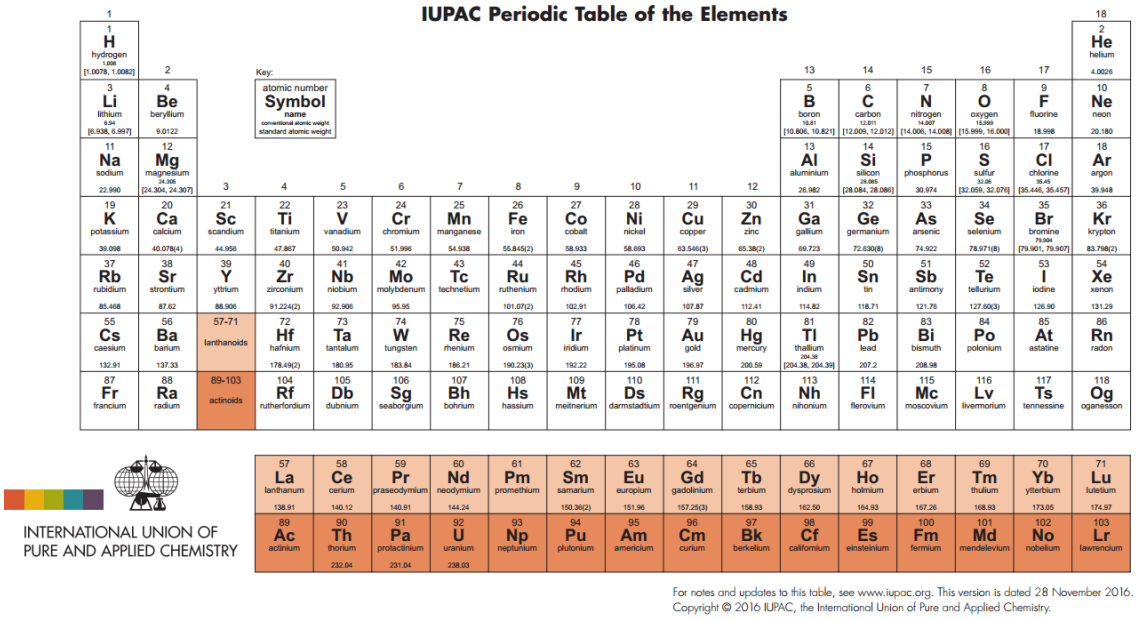

Figure 4. Periodic Table of Elements. (n.d.). Retrieved October 24, 2017, from https://www.acs.org/content/acs/en/education/whatischemistry/periodictable.html.

Since the invention of the first solid-state laser (1960) and Nd-glass laser (1961), many important successes have been achieved in diode laser pumped solid-state lasers, followed by the blooming research for new laser glasses. Specifically, high power and high energy laser system still utilizes Nd^{3+}-doped laser glasses while Yb^{3+} ones have become a huge potential replacement. In optical communication and IR lasers, Ho^{3+}, Er^{3+} and Tm^{3+} doped glasses and laser glass fibers are the main topics of development. [Ga, 06.]

Apart from Nd^{3+} and Yb^{3+} ones, Er^{3+}-doped laser glasses are one of the most important in near infra-red (IR) region. Er^{3+}-doped glass lasers have found their success in medical and rangefinder applications as 1.5 μm laser wavelength is safe for human eyes. [Ga, 06]. When excited by the laser diode at 980 nm, Er^{3+} ions are excited to $^4I_{11/2}$ energy level. This unstable state then decays to $^4I_{13/2}$ energy level via a non-radiative transition, causing emission at ~1.5 μm via a radiative transition as depicted in Figure 5.

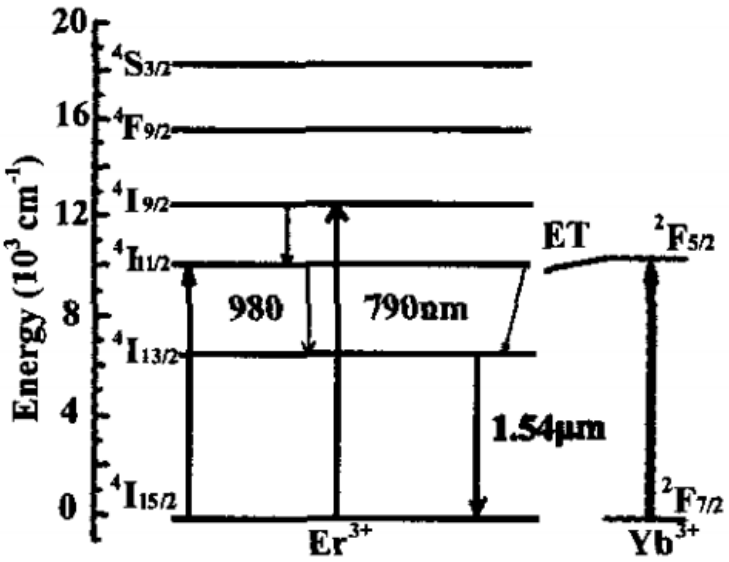

Figure 5. Er^{3+} energy level illustration showing emission transition of Er^{3+} ions in glasses pumped by 790 and 980 laser diodes [Ga, 06].

Interestingly, Er^{3+} based glass lasers can also contain Yb^{3+} as these ions act as sensitizers because of the Er^{3+} ions' weak absorption in near IR region. The Yb^{3+} ions strongly absorb the pumping light around 1 μm (especially 980 nm diode lasers pumping) before transferring the energy from their excited state $^2F_{5/2}$ to the $^4I_{11/2}$ metastable state of Er^{3+} ions, leading to intense laser emission at ~1.5 μm wavelength.

2.1.4 Upconversion in Yb^{3+}, Er^{3+} codoped materials

Another major research focus in laser glasses is glass for upconversion. Upconversion (UC) is a phenomenon where the serial absorption of two or more photons causes light emission at shorter wavelength than the excitation source. Many rare earth-doped solid materials commonly exhibit UC from the near infrared (0.7–1.6 μm), visible (0.4–0.7 μm) to UV (0.27–0.4 μm) region. [He, 01.]

The most important UC mechanisms—most effective from near IR to visible region—are energy transfer upconversion (ETU) and excited-state absorption (ESA) as illustrated in Figure 6.

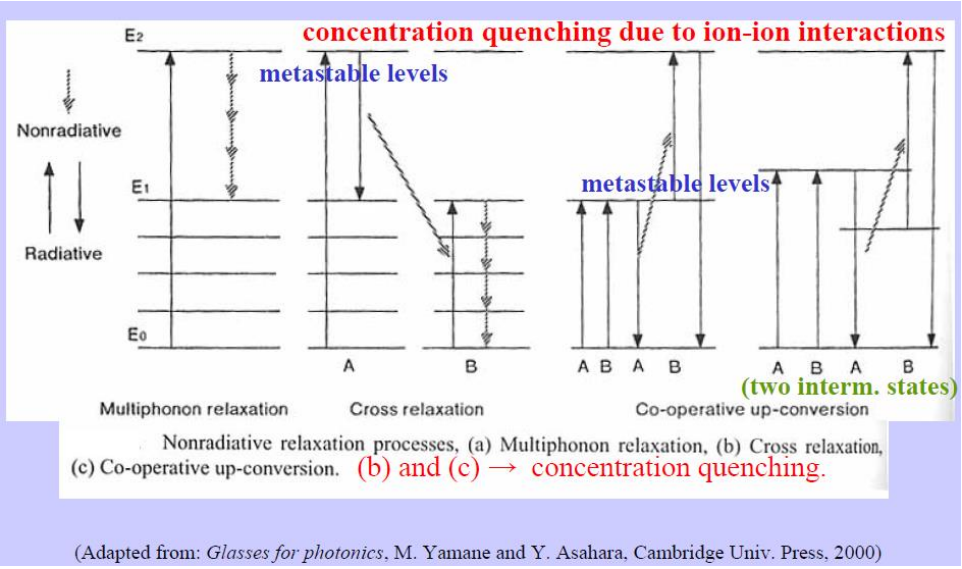

ETU

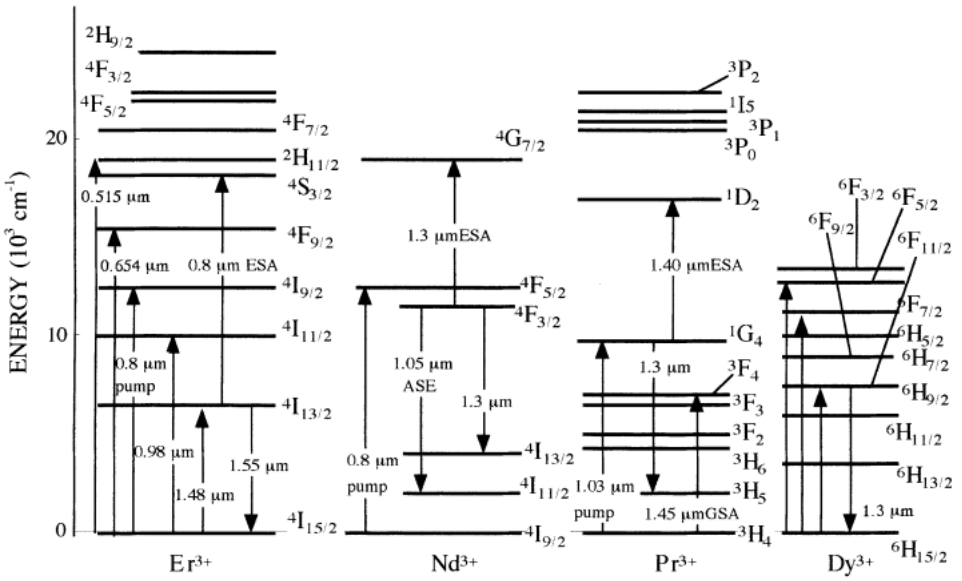

ESA

Figure 6. Schematic of different UC mechanisms [Ya, 00].

These two depend on the existence of metastable, intermediate excited states as well as a metastable emitting state. However, ETU and ESA (plus the emission process) have a competitor: non-radiative multiphonon relaxation (MR) processes. In principle, lower MR efficiency can be achieved by decreasing "the highest phonon energy of the host material". [He, 01.]

For laser glasses, energy transfer upconversion (ETU) is very common also because it is less susceptible to external influences. In its principle, an appropriate dopant works as a sensitizer and transfers the irradiated energy to other activators, which assist the upconversion luminescence. In a simple energy scheme taken as an example, the Yb-Er codoping allows the emission to be realized in the visible region with the upconversion frequency of the excitation wavelength at 980 nm. Figure 7 summarizes the possible pathways of upconversion in Yb-Er codoped laser glasses. [Tu, 15.]

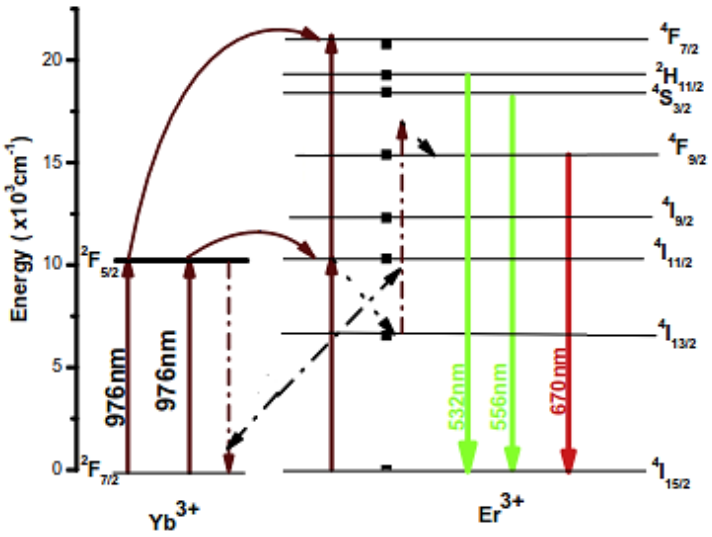

Figure 7. Upconversion of Yb-Er codoped laser glasses [Tu, 15].

In the Yb-Er codoped system, the resonance between the $^2F_{7/2}$ - $^2F_{5/2}$ transition of Yb^{3+} and $^4I_{15/2}$ - $^5I_{11/2}$ transition of Er^{3+} supplies efficient energy transfer from Yb^{3+} to Er^{3+}. When excited by 980-nm continuous pumping, Yb^{3+} and Er^{3+} absorb near-infrared (NIR) leading to the $^2F_{7/2}$ - $^2F_{5/2}$ and $^4I_{15/2} \rightarrow {}^4I_{11/2}$ upward transitions. Then, the Yb^{3+} can either transfer its energy to another Er^{3+} ion in the ground state (and boost it to $^4I_{11/2}$) or to an Er^{3+} ion already in the $^4I_{11/2}$ level exciting it to the $^2F_{7/2}$ state. Eventually, the non-radiative transition increases the population in the $^2H_{11/2}/^4S_{3/2}$ states. This leads to the corresponding green emission at 518 nm and 542 nm due to the radiative transition of ions to the ground state. At the same time, a red emission (670 nm) also occurs mostly due to the non-radiative relaxation of Er^{3+} ions to $^4F_{9/2}$ and subsequent radiative transition of ions to the ground state [Tu, 15].

Regarding the hosts, glass hosts with low phonon energy are desired when engineering new upconverters. Table 1 shows the phonon energy of several non-oxide glass hosts [Ga, 06].

Table 1. Non-oxide glass hosts and their maximum phonon energy [Ga, 06].

Glass host type	**Phonon energy (cm^{-1})**
Borate	1400
Silicate	1100
Phosphate	1200
Germanate	900
Tellurate	700
Fluoride	500
Chalcogenide	350

As can be seen, halide and chalcogenide glasses have the lowest phonon energy, while the phonon energy in phosphate glasses is high. Therefore, UC hosts are limited within halides, oxyhalides, oxysulfides and several oxides. However, chlorides, bromides and iodides are strongly hygroscopic, thus causing difficulties in applications. As a result, fluoride materials such as YF_3, $LiYF_4$, $NaYF_4$, $BaYF_5$, $LuLiF_4$, BaY_2F_8 etc. are mostly used for UC. Among those, Yb^{3+}–Er^{3+} codoped YF_3, $BaYF_5$ and $NaYF_4$ are the most effective UC materials (~980-nm excitation) for green and/or red emission; while Yb^{3+}–Tm^{3+} codoped BaY_2F_8, $LuLiF_4$ and $NaYF_4$ for blue or UV emission. [He, 01.]

The β- (hexagonal-phase) $NaYF_4$ is considered as one of the best UC hosts. The crystal lattice of this form has low phonon energy (preventing the multiphonon relaxation processes, thus lengthening lifetimes of the excited states), two distinct lattice sites for doped ions (increasing the chance of energy transfer from sensitizers to activators), as well as similar effective-ion sizes with dopants (hindering lattice defects and stress formation). [Lai, 16.] As a result, $NaYF_4$: Yb^{3+}, Er^{3+} UC nanoparticles certainly are the most effective UC luminescence material from infrared to visible region [He, 04]. In addition, this material has been researched intensively for decades, resulting in readily fabricating techniques and reliable end-products. Recently, Laihinen et al has successfully optimized the co-precipitation synthesis (the simplest method) to produce the nanoparticles with 2 times stronger UC intensity than previously obtained [Lai, 16]. Therefore, $NaYF_4$: Yb^{3+}, Er^{3+} UCNPs are selected for doping in this thesis work.

2.2 Glass-ceramics

As mentioned previously, there is no definite order in glass structure. So, the modifying ions are located in multiple different local environments. In doped glasses, RE-ions occupy equivalent positions as the modifying ions leading to the broadening of the absorption and of the emission spectra. Also, the RE-ions possess larger non-radiative transition possibility in glasses than in crystals and therefore exhibit lower emission efficiency in glasses than in crystals. To increase the emission efficiency, the RE ions must be orderly arranged as shown in Figure 8 which depicts this difference between Nd ions doped in phosphate glass and in crystal (YAG). [Ya, 00.]

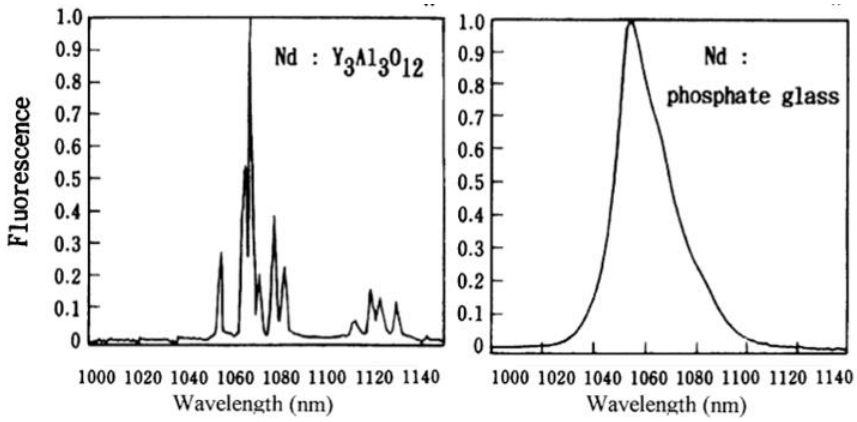

Figure 8. Nd ions' emission spectra in YAG crystal (left) and in phosphate glass (right) [Ya, 00].

Therefore, there has been a constant interest in developing new RE doped glass-ceramics. Such materials can be obtained using different techniques which are discussed in the following sections.

2.2.1 Nucleation and growth

To control the crystal growth in glass ceramics, one must well-understand the nucleation and growth mechanisms. There are two common ones: volume and surface nucleation. In volume nucleation, there are homogeneous and heterogeneous mechanisms. For the former, the formation ΔG of one spherical nucleus having a radius equal to r is described by following equation:

$$\Delta G = -\frac{4}{3}\pi r^3 \Delta G_v + 4\pi r^2 \gamma + \Delta G_E, \qquad [1]$$

where ΔG is the free-energy change per unit volume corresponding to the new phase formation, γ the interfacial energy per unit area of the nucleus's new surface and ΔG_E the elastic distortion energy. [Hö, 03.]

The glass-ceramics development is commonly controlled by heterogeneous nucleation. Heterogeneous mechanism is involved when nucleation agents are added to the base glassy matrix as a special catalyst for nucleation. A spherical-cap nucleus is formed on the catalytic substrate by a contact angle (θ). The critical heterogeneous nucleation formation ΔG_H^* is lower for smaller contact angles θ as described by:

$$\Delta G_H^* = \Delta G^* f(\theta), \quad [2]$$

in which ΔG^* is the critical nucleus formation (the thermodynamic barrier) and $f(\theta) = \frac{1}{4}(2 + \cos\theta)(1 - \cos\theta)^2$.

According to the [2] equation, when the catalytic substrate is fully wetted by the nucleus and the θ is approaching 0 degree, the nucleation barrier is significantly reduced. Therefore, the efficiency of heterogeneous nucleation can be notably increased by epitaxy (a relationship of similar crystal lattice geometry) in the middle of the substrate and nucleus. The epitaxy can also be increased by the bonding state, structural defects and the nucleant-surface-vs-alien-nuclei coverage level. [Hö, 03.]

The nucleation rate kinetics I as a function of time t are described by the following formula:

$$I = I_0 \exp(\frac{-\tau}{t}), \quad [3]$$

in which I_0 is the rate of steady state nucleation, τ is the time lag of non-steady state (a time before reaching the rate of steady state).

I_0 is expressed as:

$$I_0 = A \times \exp(\frac{\Delta G^* + \Delta G_D}{kT}), \quad [4]$$

where ΔG_D is the nucleation kinetic barrier, k the Boltzmann's constant and A a pre-exponential factor.

I_0 is related to the glass phase viscosity by an inverse variation. The nucleation action can be characterized via experimentally determining the rate of nucleation (I) and the nucleus number (N) as a function of heat treatment time in isothermal states. As a result, the I(t) and N(t) functions can also be ascertained at various temperature as well as the lag time τ. [Hö, 03.]

In volume nucleation, micro-immiscibility can play an important role as it affects the phase separation. In the base glass, phase separation enables the possibility to reach early volume crystallization or postpone it via changing the matrix composition, thus eliminat-

ing unwanted behaviors such as surface or out-of-control volume crystallization. Additionally, phase separation can promote the formation of a low-viscosity, homogeneous-crystallized phase as well as either concurrently or subsequently heterogeneous crystallization of the matrix. Finally, crystallization-preferred sites and interfaces are formed via phase separation. Interestingly, phase separation can also be controlled by reducing the nucleation kinetic barrier ΔG_D in equation [4], thus permitting the preferred main crystals to be directly and quickly formed in the droplet phase.

It has been found that nucleating agents such as fluoride, P_2O_5, Fe_2O_3, TiO_2, ZrO_2, Ta_2O_5 and WO_3 help to create a noteworthy microphase separation in many systems, effectively developing glass ceramics. [Hö, 03.]

Although most glass ceramics involve volume nucleation, there are some glasses that cannot undergo controlled crystallization via this mechanism but only through a more difficult one—surface nucleation. Surface nucleation control can be achieved via the glass surface's tribochemical activation. Another option is seeding the glass surface—adding fine-powdered glass either of similar compositions or heterogeneous particles. Finally, the elastic strain ΔG_E in equation [1] may play an important role in surface nucleation as well [Hö, 03]. However, this conventional technique has many shortcomings. Firstly, it does not always lead to the volumetric precipitation of RE-containing crystals as explained in [Ge, 17]. There are inherent limitations about integrating RE ions into the in-situ growing crystals with relatively exact/maximum concentrations as well as controlled order at each crystalline site. Secondly, this method is unable to produce RE-doped nanocrystals with core-shell and heterogeneous nanostructures, thus limiting the ability to design nanoscale-level properties. Finally, further heat treatments (i.e. fiber drawings etc.) can overgrow the already-optimal crystals, reducing the number of subsequent applications.

2.2.2 Direct doping method

Besides the classic one-melt glass-ceramics method, a new technique has been successfully experimented lately by Zhao et al [Zh, 16]—the direct doping of particles into the glass melt. The theoretical results of these methods are depicted in Figure 9b and c, respectively.

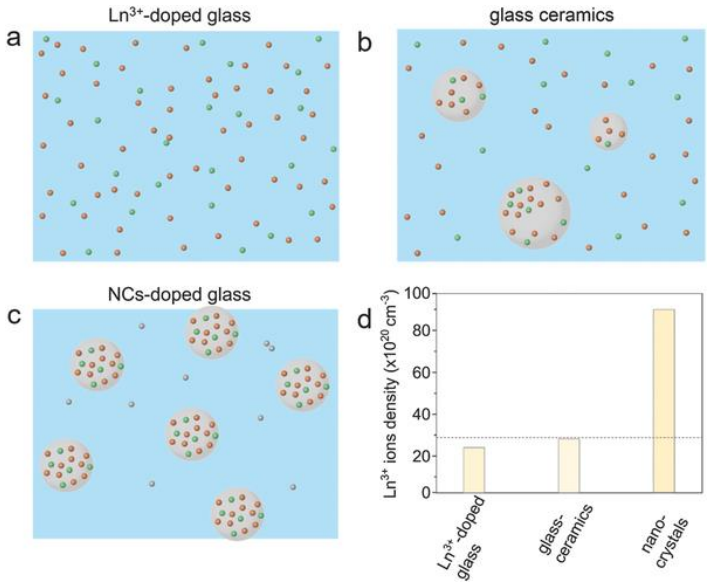

Figure 9. a–c) Theoretical phase results from different fabricating methods and d) the comparison [Zh, 16].

In the direct doping method, desired RE-containing nanocrystals (previously synthesized with high precision via solution chemistry) are incorporated in the glass matrix only after the glass has been melted completely. The theoretical result from the direct doping of particles is displayed in Figure 9c. Theoretically, the pre-synthesized particles with RE bring significant improvements to the resulting glasses due to the precise control of the nanocrystals' parameters. As compared in Figure 9d, the direct doping method clearly surpasses other fabricating techniques in terms of RE ion concentration. As already mentioned, the technique has been applied successfully by Zhao et al. to dope telluride glasses with $LiYF_4$ nanoparticles, yielding fascinating results. Nevertheless, the authors reported 30–60% loss of the nanoparticles in the glass, indicating a major room for improvement [Zh, 16].

Based on the above knowledge, one main purpose of this thesis is to explore the usefulness of the direct doping methods on another glass system and optimize the particle dispersion. As explained in [Zh, 16], it is crucial to identify a suitable temperature for doping and dispersing the particles in the glass melt to succeed in doping the glasses homogenously with particles. The particles need to be, of course, thermally stable at this doping temperature to ensure the survival of the particles within the glass during the glass preparation. Therefore, as explained in [Ng, 17], the first step is to identify a glass composition, the doping temperature of which could be lower than the particles upper limit of the doping temperature. The second step is to determine two parameters in order to prepare glasses with homogeneous particle dispersion: the doping temperature at which the particles are added and the dwell time before casting the glasses to ease the dispersion of the particles but in the same time the dissolution of the particles in the glass melt can occur if the dwell time is too long.

3. MATERIALS AND RESEARCH METHODOLOGY

3.1 Melting of the glasses and particles-containing glasses

3.1.1 Glasses

Glasses with the composition of $45P_2O_5$—$(55\text{-}x)Na_2O$—$xNaF$ (in mol%) were prepared with x= 0, 2.5, 5, 7.5 and 10. The raw materials included $Na_6O_{18}P_6$, Na_2CO_3 and NaF; they were purchased from the following companies: Alfa-Aesar (technical grade), Sigma-Aldrich (≥99.5%) and Sigma-Aldrich (99.99%), respectively. These chemicals were used directly without purifying steps.

From the glass composition, the amount of raw materials was calculated and weighed to prepare an 8-gram glass batch. To increase the glass batch homogeneity, the precursors were mixed in a ceramic mortar using a ceramic pestle before pouring the batch into a platinum/quartz crucible.

The Na_2O-containing glass batches were, first, heated to 300°C using a 15°C/min ramping rate in normal lab-condition atmosphere and held at this temperature for 15 minutes to release CO_2 gas from the chemicals. Then, the glasses were melted at 750°C for 10min. After quenching, the glasses were annealed at 40°C below their respective glass transition temperature to release the stress from the quench.

3.1.2 Particles containing glasses

The microparticles (MPs) used for the optimization of the direct doping method are $CaAl_2O_4$: Eu^{2+}, Dy^{3+}, from Jinan G.L. New Materials, China, BG-01.

The nanoparticles (NPs) have the composition of $NaYF_4$: Yb^{3+}, Er^{3+}, in which the atomic percentage of Yb^{3+} and Er^{3+} are 17 at% and 3 at%, respectively. The NPs were synthesized by the co-precipitation method in collaboration with Dr. Mika Lastusaari from Turku University (Finland). In this synthesis, solid NaF was solvated to distilled water and mixed with a solution containing YCl_3, $YbCl_3$ and $ErCl_3$. This mixture was stirred for 1 hour at room temperature. Subsequently, it was washed with water (3 times) and ethanol (1 time), followed by a drying period in vacuum desiccators (room temperature). Finally, the powder was dried under a static N_2–H_2(10%) gas sphere. [Lai, 16.]

Particles-containing glasses were obtained from the direct doping method. Prior to the melting at 750°C for 5minutes, the Na_2O-containing glass batches were, first, heated to

300°C for 15min as explained in the previous section. After that, the batch was manually swirled for nearly 5 seconds (to homogenize the melt) before being returned to another furnace which was already at the doping temperature (i.e. 575, 600 or 650ºC). A platinum lid was used when preparing the F-containing glasses to prevent the evaporation of F during the glass preparation. After 20 minutes at this doping temperature, the particles were added into the molten glass. The mixture was then held at the doping temperature for a defined duration, from 3 to 10 minutes. Subsequently, the mixture was slightly swirled again (for ~1 second) before being casted into a brass mold. After quenching, the glasses were annealed at 40ºC below their respective glass transition temperature to release the stress from the quench. As the glasses are hygroscopic, they were finally stored in a desiccator.

3.2 Scanning Electron Microscope (SEM)

Scanning Electron Microscope (SEM) employs accelerated electrons to image and analyze a sample's area by collecting secondary electrons (inelastic scattering between the beam electrons and the sample's K-shell electrons) and backscattered electrons (elastic-scattered beam electrons with the sample's atomic nuclei; the scattering probability corresponds to the atomic mass—the composition). As shown in Figure 10, the thermal electrons are generated from the gun and accelerated by an electric field before being directed to the sample by magnetic coils.

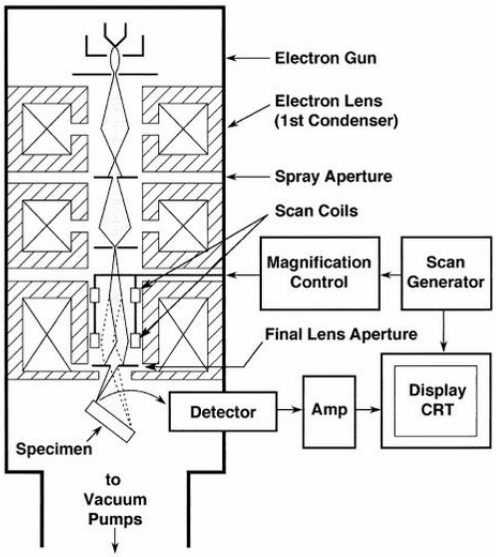

Figure 10. Illustration of a SEM electron column [Go, 03].

The produced (secondary) electrons are collected by the detector to yield topography information. Meanwhile, elemental characteristic K_α and K_β X-rays can also be generated at the same time as the secondary electrons using an Energy-dispersive X-ray Spectroscopy (EDS). The X-ray emissions are used to identify and map the sample's elemental

composition. All these actions take place in vacuum to prevent gas molecules interfering with the electron beam. [Go, 03.]

In this study, a Carl Zeiss Crossbeam 540 Gemini Scanning Electron Microscope combined with an x-Max N 80 EDS, Oxford Instruments Energy Dispersive X-ray Spectroscopy was used to image and analyze the glass samples' composition. The accelerating voltages were 15 and 20 kV for NPs and MPs samples, respectively. The elemental analysis' accuracy is ±1.5 mol%. The polished samples were carbon-coated to improve the image contrast before performing the measurements. The obtained EDS data were saved in ACII format.

3.3 Physical and thermal properties

3.3.1 Density Measurement

The density of the polished glasses was determined using the Archimedes' method. Ethanol was chosen as the immersion liquid due to the glass's reaction with water. The measurement was done using an OHAUS Adventurer Analytical scale along with its own kits (submerged cradle etc.). The glass pieces were weighed first in air and then in ethanol, considering the temperature of the liquid at the time. Subsequently, the density was calculated using the following equation:

$$\rho_{glass} = \frac{m_{in\ air}}{\Delta m}\rho_{ethanol} \quad [5]$$

where ρ_{glass} and $\rho_{ethanol}$ are the density of glass and ethanol, respectively, $m_{in\ air}$ is the mass of the glass sample weighed in air, and Δm is the mass difference when weighed in air and in ethanol. [Ma, 16.]

The accuracy of the measurement is ±0.02 g/cm^3.

3.3.2 Differential Scanning Calorimetry (DSC)

Differential Scanning Calorimetry is "a technique where the difference between heat flow rates into a sample and a reference material is measured" [Le, 14]. The schematic diagram of a DSC device is depicted in Figure 11. Individual heaters are used to heat the sample and a reference. These two are also kept at similar temperature by a system controlled by Pt (platinum) resistance thermometers. Non-identical amounts of heat are generated by the specimens, then the power-input differences to the heaters are recorded, generating peaks in the corresponding diagram (Figure 11b). The resulting curve can be used to quantify important data such as specific heat or heat of reaction. [Ke, 80.]

a)

b)

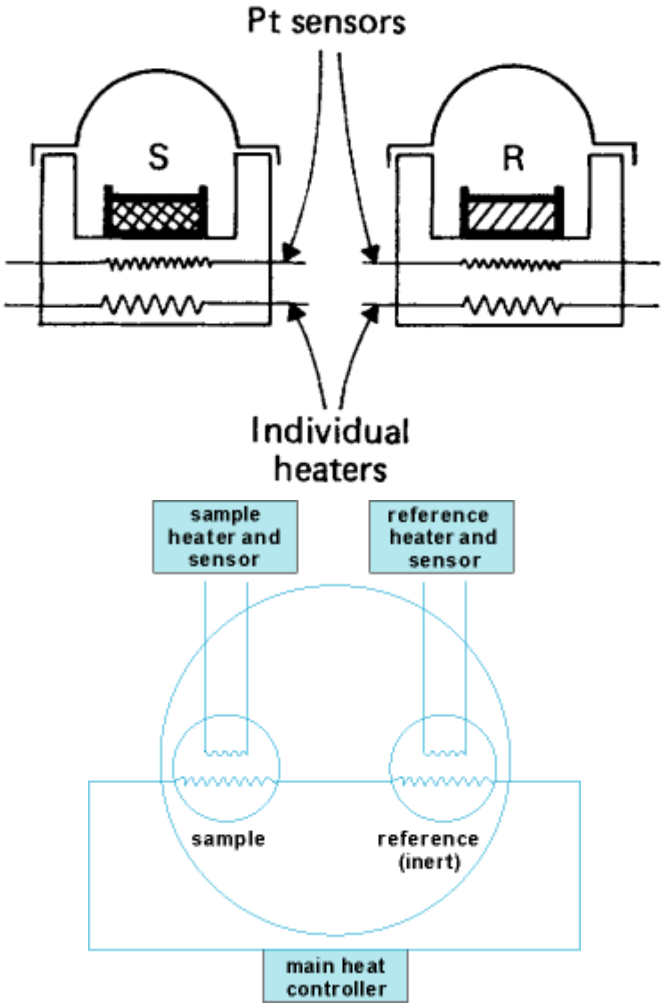

Figure 11. Illustration of DSC's a) specimen holder [Ke, 80] and b) heating-sensing units [Je, 14].

In this thesis work, a NETZSCH STA 449 Differential Scanning Calorimetry apparatus was used to measure the glass's transition (T_g) and crystallization (T_p and T_x) temperatures. A part of each glass samples was crushed into fine powder which was heat treated in a platinum pan with lids at 10°C/min heating rate from 40 to 500°C.

Figure 12 depicts the thermogram of the glass with x=0, taken as an example. The T_g was taken at the inflection point of the endotherm which is the first derivative of the DSC curve. On the other hand, the onset (T_x) and the peak (T_p) crystallization temperatures were obtained at the inflection point and the highest point of the first exothermic peak, respectively. The accuracy of these measurements is ±3°C.

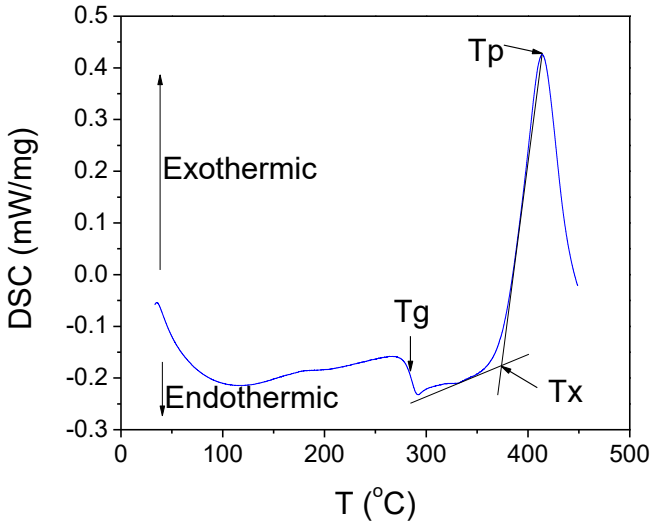

Figure 12. Thermogram of the glass.

3.3.3 Viscosity measurement

The glass viscosity depends on temperature as illustrated in Figure 13.

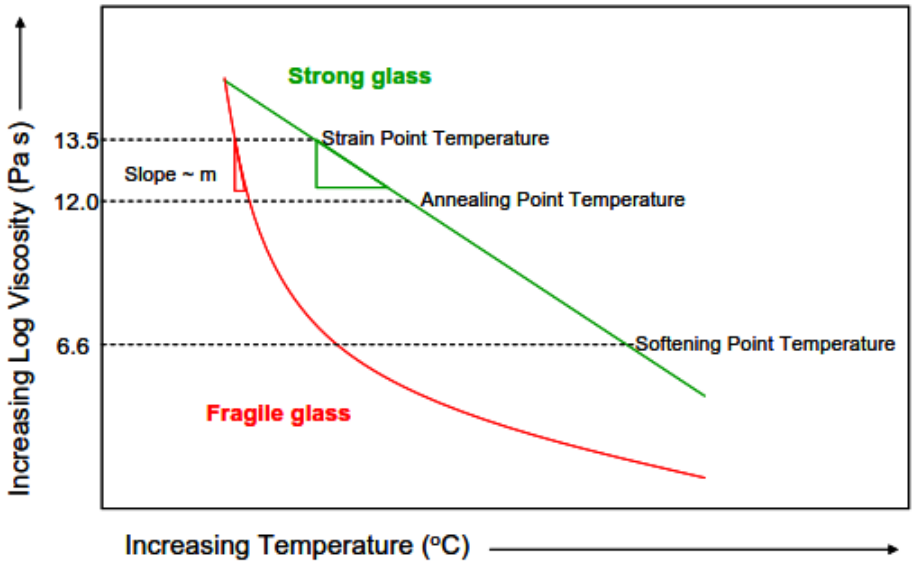

Figure 13. Typical temperature-viscosity curve of fragile and strong glasses [Ga, 08].

A beam-bending viscometer (BBV) was used to measure the viscosity in the (Log11—Log13 Pa.s) range. The instrument was a BÄHR Thermoanalyse, type VIS 401 as shown in Figure 17. The measurement was conducted under the test protocol ASTM C-1351M and performed at the Otto Schott Institute of Materials Research, Friedrich Schiller University in Germany in collaboration with Delia Brauer.

Figure 14. Beam-bending viscometer BÄHR Thermoanalyse VIS 401.

The glasses with x=0 and 10 were cut in 4 x 5 x 50mm bars which were mounted on 3-point beam-bending quartz-glass tubes (2) inside the heating chamber (3). The metal rod under the quartz tube (2) is a part of a balance (1) which can be used to apply higher force on the sample by adding more weights (50—250g). Before each measurement, this metal rod is calibrated so that it slightly touches the sample at room temperature. Upon heating using a 10°C/min rate, the loaded metal rod deforms the sample as sample's viscosity decreases. This bending deformation (distance by which the sample's center is moved in a 90-degree angle to its axis) is measured via the metal rod's angle on the balance by an inductive displacement transducer. Finally, the viscosity is calculated at each temperature point using the following equation:

$$\eta = \frac{gL^3}{1440 I_c \left(\frac{dh}{dt}\right)} \left(M + \frac{\rho A L}{1.6} \right) \qquad [6]$$

where η is the viscosity (Pa.s); M—the applied load (g), dh/dt the midpoint deflection rate of test beam (cm/s), g the acceleration of gravity (980 cm/s^2), I_c the cross-sectional moment of inertia (cm^4), ρ the density of glass (g/cm^3), A the cross-sectional area of the beam (cm^2) and L the support span (cm) [ASTM, 03].

The glass viscosity in the softening range (Log5—Log 8 Pa.s) was measured using a parallel-plate viscometer—Model PPV-1000— shown in Figure 15 in College of Optics and Photonics (CREOL), University of Central Florida, USA.

Figure 15. The parallel-plate viscometer for viscosity measurement [Or, 07].

The measurement followed the test protocol ASTM C-1351M. In this test, the glasses with x=0 and 10 were prepared in disk with a diameter of 10mm and a thickness of at least 5mm. Those disks were positioned between two parallel platinum-foil-protected Inconel plates. Each disk was applied a standard load while being heated at a rate of 5 ^{o}C/min. The specimen's height was monitored during this heating process as a function of its temperature. [Ti, 10.] From this data, the glass viscosity was using the following equation:

$$\eta = 2\pi \frac{Mgh^5}{30V(dh/dt)(2\pi h^3 + V)} \qquad [7]$$

where V is the volume of the specimen (cm^3) while h (cm) stands for the specimen thickness at time t (s) [ASTM, 02].

Until now, these measurements are still unable to be conducted at temperatures much lower than the glass transition because of the long structural relaxation period [Ma, 09]. So far, such data has been only estimated via mathematic models. The classic and most common model is the Vogel–Fulcher–Tammann equation:

$$log_{10}^{\eta} = -A + \frac{B}{T - T_o}, \qquad [8]$$

with A, B and T_o are fitting parameters from the measured viscosity information [Sc, 92].

3.4 Optical properties

When developing optical glasses, it is crucial to measure their optical properties. In light absorption principal, an electron may absorb a photon having equivalent energy to an

electronic transition in an electron-photon collision. While the electron can transition itself to an excited level, the photon is absorbed and the light intensity is reduced. A spectrophotometer measures this reduction as a function of the wavelength. Figure 16 below depicts a typical spectrophotometer.

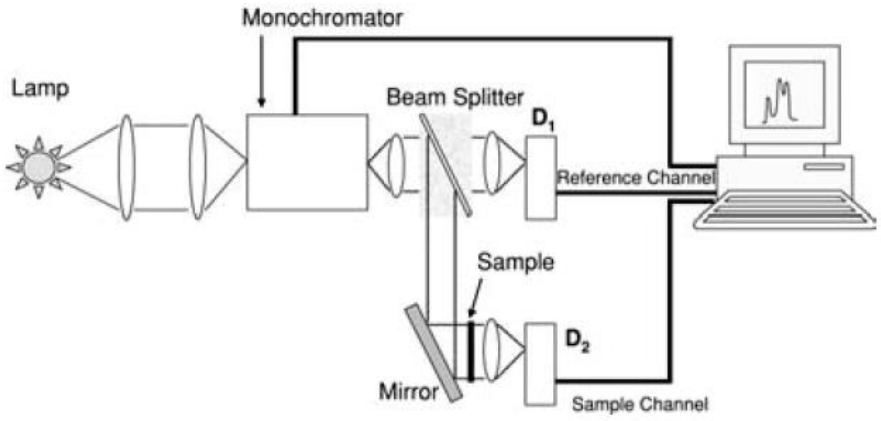

Figure 16. A typical spectrophotometer and its main parts [So, 05].

The monochromator selects a narrow spectral band from the light source (lamp) and let it pass to a beam splitter, which splits the band in to two. One beam moves freely to a detector (reference beam—I_0), while the other (I) passes through a sample, loses a degree of intensity before reaching another detector. The computer collects the intensity (I_0 and I) from the detectors and provides the output results [So, 05]. The absorbance (A) is calculated from the ratio (I_0 /I) as following:

$$A = \log({}^{I_0}/_{I}) \qquad [9]$$

The absorption coefficient is then calculated from the Beer Lambert law:

$$\alpha = \frac{\ln(10)}{L} A \qquad [10]$$

where L is the sample's thickness (cm).

Finally, the absorption cross-section $\alpha(\lambda)$ (cm^{-1}) is then estimated at ±10%.:

$$\alpha(\lambda) = \ln(10)\frac{A}{NL} \qquad [11]$$

with N is the rare-earth ion concentration ($ions/cm^3$) calculated from the glass density and the batch composition. [Lo, 17.]

In this work, the absorption and transmission spectra were measured using an UV-Vis-NIR spectrophotometer (UV-3600 Plus, Shimadzu) from 190 to 1700 nm with 0.5 nm

interval, single scan mode and fast, medium or slow scan speed. The glasses were polished and their thickness was determined using a digital caliper with an accuracy of ±0.05 mm.

3.5 Luminescence properties

The luminescence properties of the glasses were measured at Turku University (Finland) in collaboration with Dr. Mika Lastusaari.

3.5.1 Persistent luminescence (PeL)

Persistent luminescence (PeL), or afterglow, is a phenomenon where emissions (visible, UV light, X-rays etc.) are exhibited after ceasing excitation [Ha, 57]. Interestingly, its definition has not been clearly clarified due to too many confusing terms such as fluorescence, phosphorescence, long-lasting luminescence… just to name a few. However, there are two names that should not be confused with PeL. Firstly, PeL is not thermoluminescence (a more general term) but a special instance of thermally stimulated luminescence at a specific temperature [He, 12]. Secondly, there is an absolute difference between PeL and phosphorescence as the latter refers to long-lifetime luminescence originated from the forbidden transitions within the corresponding center [Bl, 94]. In fact, PeL materials stores excitation energy in intrinsic traps such as defects [Ha, 10], aliovalent codoping [Br, 11] etc.

There have been thousands of PeL materials dating back to even 1000 years in China [Ru, 37]. Nonetheless, the major flourishing period of their researches and applications only began since the middle of 1990s when effective Eu^{2+}, R^{3+} codoped materials (blue-light emitting $CaAl_2O_4:Eu^{2+}$, Nd^{3+} [Ya, 97] and green-light emitting $SrAl_2O_4:Eu^{2+}$, Dy^{3+} [Ma, 96]) were introduced. Other commercially successful PeL materials include $Sr_2MgSi_2O_7:Eu^{2+}$, Dy^{3+} [Li, 01] and ($Sr_4Al_{14}O_{25}:Eu^{2+}$, Dy^{3+}) [Li, 02] which are found to have enhanced reliability against moisture, as well as $Y_2O_2S:Eu^{3+}$, Mg^{2+}, Ti. All of them have outstanding afterglow up to over 1 day.

The most modern PeL mechanism for Eu^{2+}-doped materials are presented in Figure 17. Upon charging, electrons are moved from the ground state [$4f^7(^8S_{7/2})$] to the excited states [$4f^65d^1(^2D)$]. Thanks to the thermal energy (kT), Eu^{2+} long lifetime emission of $4f^65d^1(^2D) \rightarrow 4f^7(^8S_{7/2})$ and the closeness of Sr_3SiO_5's conduction band, several electrons can bypass the excited level of Eu^{2+} to the host's conduction band. They advance easily in this band until being trapped by defects. When decharging begins upon stopping UV charging, the thermal energy absorption permits the trapped electrons to return to the conduction band, populating the $4f^65d^1(^2D)$ states of Eu^{2+}. Eventually, the non-radiative and radiative relaxation of the ion generate the PeL. Also, the electrons may be re-trapped in each step of the decharging, thus extending the period of PeL. [He, 12.]

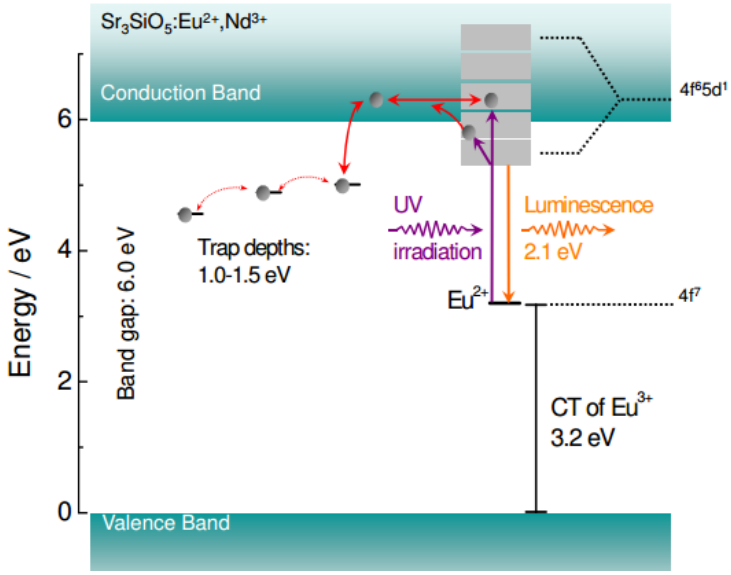

Figure 17. Schematic diagram of one of the most advanced PeL mechanism for $Sr_3SiO_5:Eu^{2+}$, Nd^{3+} [Hö, 11].

The persistent luminescent spectra of the MPs- containing glasses were measured using a Varian Cary Eclipse Fluorescence Spectrophotometer coupled with a Hanamatsu R928 photomultiplier (PMT). The samples were irradiated with a UVGL-25 (4W, λ_{exc}=254 nm) lamp for 5 minutes. The measurement was taken 1 minute after ceasing the excitation. The luminescence intensity was obtained by integrating the area under the emission curve. The measurements were performed at room temperature.

A schematic of the spectrofluorometer used for the measurement is depicted in Figure 18. In this instrument, motorized monochromators are usually equipped to concurrently select the excitation and emission wavelengths for automatic wavelength scanning. The fluorescence is recorded by photomultiplier tubes (PMT) [La, 06].

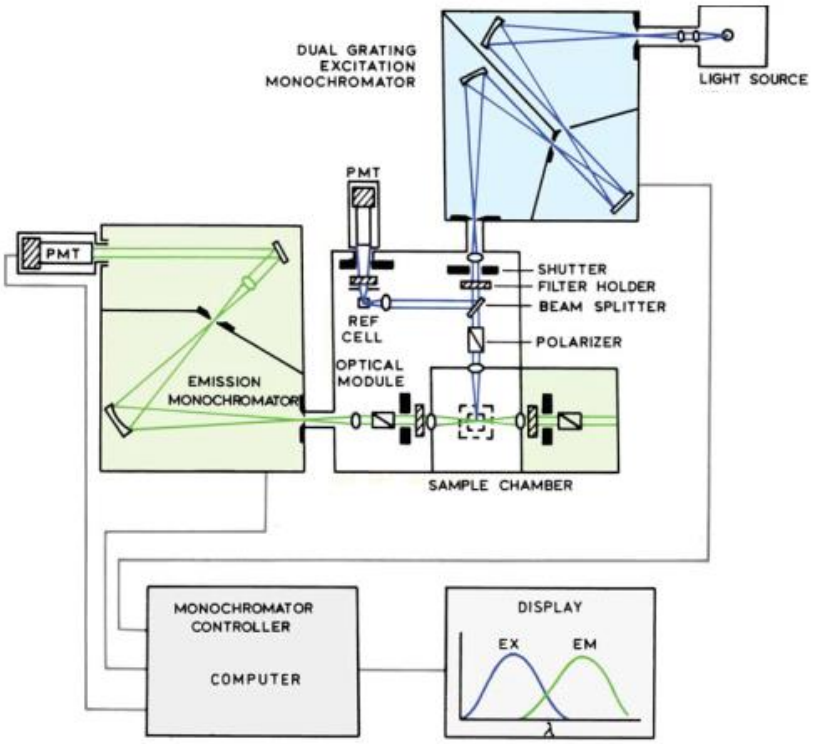

Figure 18. A typical spectrofluorometer's schematic diagram [La, 06].

3.5.2 Conventional luminescence (PL)

Conventional luminescence (or photoluminescence—PL) is the impulsive light emission from a RE-doped material when it is optically excited. Theoretically, when the material is excited by adequately energetic light, photons are absorbed—resulting in electronic excitations. Ultimately, relaxation occurs for those excitations, electrons then go back to the fundamental position—"the ground state". If the relaxation is a radiative one, the light emissions are known as photoluminescence (PL) and can be recorded for analysis. The PL spectrum gives information about the transition energies (to ascertain electronic energy levels); while its intensity can be used to determine the radiative–nonradiative recombination's relative rates. Additionally, PL measurement is wildly utilized to characterize surfaces. The method is uncomplex, multipurpose and nondestructive; however, it depends heavily on the light emitting ability and poses problems for interface-density and impurity-state assessment. [Gf, 00.]

The conventional luminescence spectra of the MPs-containing glasses were measured using a charge-coupled devices (CCDs) camera (Avantes, AvaSpec-2048x14). As depicted in Figure 19, CCDs are imaging detectors and widely used in combination with spectrofluorometers.

a)

b)

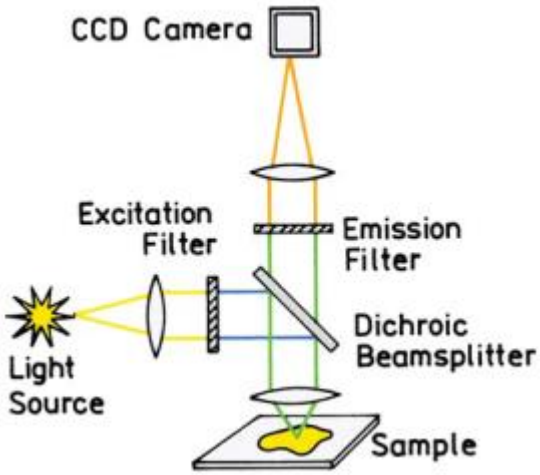

Figure 19. A typical CCD spectrofluorometer (a) and conventional luminescence setup (b) [La, 06].

The excitation source was a Nd: YAG pulse laser (λ_{exc}=266 nm, 8 ns, TII Lotis) with 50 ms integration time and 10 averaging. All the measurements were performed at room temperature from glasses crushed into powder. Figure 20 summarizes the basic setup of a PL measurement.

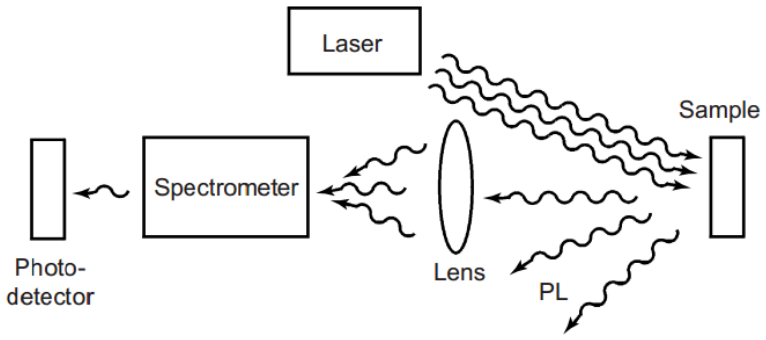

Figure 20. Typical diagram of a PL measurement [Gf, 00].

In principle, the sample is pointed by a laser—tuned to a wavelength close to the sample's bandgap energy. When the laser beam excites the sample, PL occurs—light is emitted from the sample at wavelengths depending on the sample composition. The reflected laser beam and the PL emission transmit in different directions by specially orienting the sam-

ple. The emitted light is guided into a fiber optic cable and a spectrometer. The spectrometer has a diffraction grating for diffracting various wavelengths in different directions toward an array of photo-detectors. Theses detectors measure each wavelength component's intensity. The information is interpreted and a PL spectrum is generated [Gf, 00].

3.5.3 Upconversion

The upconversion of NPs-doped glasses was measured using a 975-nm pump with a NIR fiber-coupled laser diode IFC-975-008 (Optical Fiber Systems, Chelmsford, MA). The output signals were gathered by a fiber-optic spectrometer (AvaSpec-2048x14) with 350 ms integration time and 100 averaging. The schematic diagram of the spectrometer is presented in Figure 21. All the measurements of the crushed NPs-doped glasses were performed at room temperature.

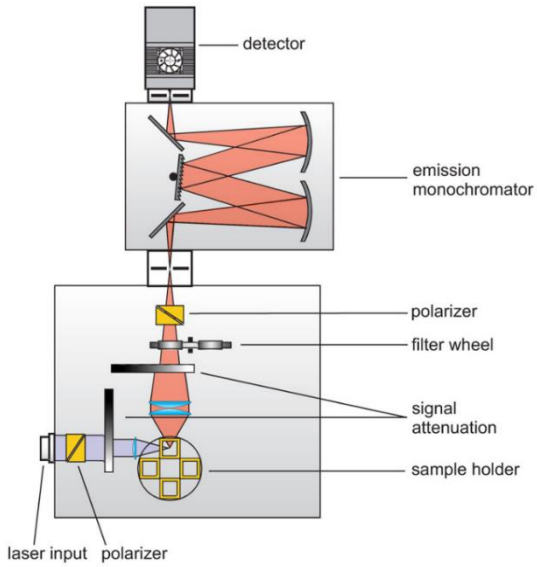

Figure 21. A classical spectrometer set-up for upconversion study.

3.6 Structural properties

The structural properties of the glasses were analyzed using IR and Raman spectroscopies.

3.6.1 IR spectra

Infrared spectroscopy provides molecules' structural information in the sample from their vibrational energy level. [Pa, 09.] In the FTIR device (Figure 22), the mirror is moveable for the IR detector to identify an interferogram of the source's spectra. This interferogram is a Fourier transform consisting of intensity periodic changes from constructive and de-

structive interference. It can be numerically reconstructed on computer, yielding the original spectra. In addition, FTIR can also determine the samples' absorbance when measuring with and without the sample. [So, 05.]

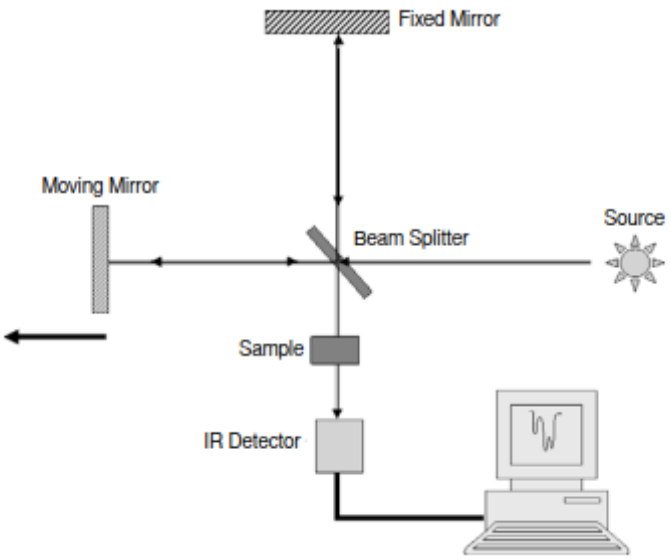

Figure 22. A typical FTIR spectrometer and its main parts [So, 05].

In the ATR mode, the beam is guided into a high-refractive crystal, bounced between surfaces and exiting to the detector. At the crystal-sample boundary, the beam undergoes total internal reflection while creating an evanescent wave beyond the crystal surface. The wave travels a few micrometers into the sample and is absorbed by the sample. This absorption of the evanescent wave is then measured by the detector [Pe, 05].

The IR spectra of the glasses were measured using a Perkin Elmer Spectrum FTIR2000 spectrometer with Attenuated Total Reflection (ATR) mode between 600 and 2000 cm^{-1}. The resolution was 2 cm^{-1} and obtained from 8-scan accumulation.

3.6.2 Raman spectra

Raman spectroscopy is another common technique used to detect vibrational, rotational and other low-frequency modes in a system. The technique relies on the inelastic scattering of photons and changes in a molecule's polarizability. The molecule's sinusoidal vibration changes its polarization, making the photon loses or gains energy that is equivalent to the vibrational energy spacing in the molecule. Consequently, this provides a structural characteristic for identifying the corresponding molecules [Ba, 01].

a)

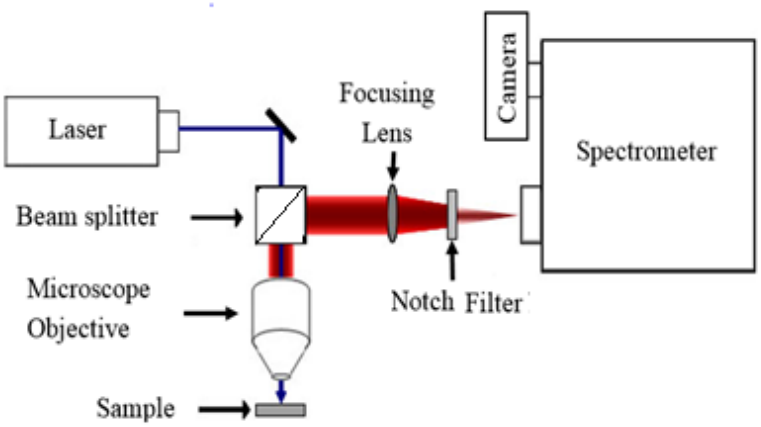

b)

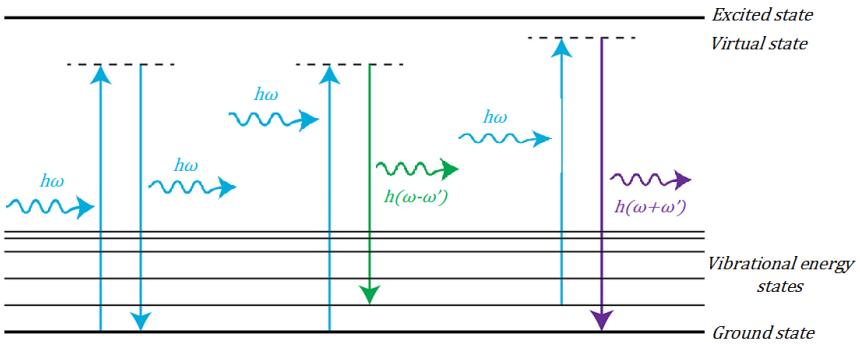

Figure 23. Typical Raman measurement setup (a) and the principle of Raman spectroscopy (b) [Ba, 01].

The Raman spectra were measured between 0 and 2000 cm^{-1} at room temperature using a Thermo Scientific™ DXR™ 2xi Raman Imaging Microscope, whose setup and working principle are illustrated in Figure 23a and b, respectively. The laser's power was 500 mW. The exposure time was 5 seconds/pixel and the data was averaged 10 times. The resolution of the spectra was 2 cm^{-1}.

4. RESULTS AND ANALYSIS

4.1 Glass selection

The first step of the research is to identify a host glass in which the particles can be dispersed without being degraded/corroded. As explained in [Zh, 16], there are 2 parameters to optimize: the doping temperature at which the particles should be added in the glass and the dwell time before quenching the glass to allow the dispersion of the NPs in the glass. The doping temperature should be lower than the particles' dissolution points but high enough to disperse them effectively (low viscous melt): Zhao et al suggested that the viscosity of 5 Pa.s—"like honey at room temperature"—is the lower limit for doping in tellurite glasses [Zh, 16]). In other words, to ensure the survival of particles, the host-glass-melting temperature cannot be higher than the particles' decomposition temperature which was reported at 750°C in [La, 17]. Additionally, the host glass must be stable to avoid crystallization when adding the particles. A glass is suspected to be stable against crystallization when ($\Delta T = T_x - T_g$) is higher than 100°C [REF].

Based on these preliminary conditions, glasses with the composition $90NaPO_3$-(10-x)Na_2O-xNaF with x=0, 2.5, 5, 7.5 and 10, in mol% were selected. The glasses were prepared using a melting temperature of 750°C. The density and the thermal properties of the glasses are reported in Table 2.

Table 2. Density and thermal properties of the glass samples in the system.

x	T_g [°C] (±3°C)	T_x [°C] (±3°C)	$\Delta T=T_x-T_g$ [°C] (±6°C)	T_p [°C] (±3°C)	Density [g/cm^3] (±0.02 g/cm^3)
0	284	374	90	414	2.47
2.5	272	378	106	415	2.47
5	264	374	110	403	2.47
7.5	255	368	113	395	2.46
10	246	356	110	402	2.45

The glass transition (T_g), the onset of crystallization (T_x) and the peak of crystallization (T_p) temperatures decrease when increasing x. An increase in x increases ΔT, the temperature difference between T_x and T_g, which is an indicator of the glass resistance to crystallization. Therefore, the F-containing glasses are stable against crystallization. Finally, the glasses' density remains almost unaffected by the composition changes.

The viscosity graph is presented in Figure 24.

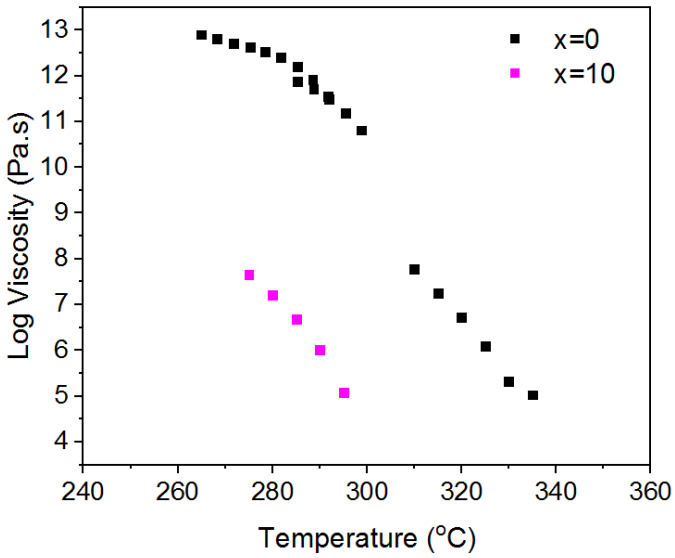

Figure 24. Viscosity of the glasses with x=0 and 10.

Based on the data, the viscosity of the glass shifts to lower temperature when x increases in agreement with the thermal properties listed in Table 2.

The IR spectra are presented in Figure 25. The spectra are normalized to the band at 1080cm^{-1}.

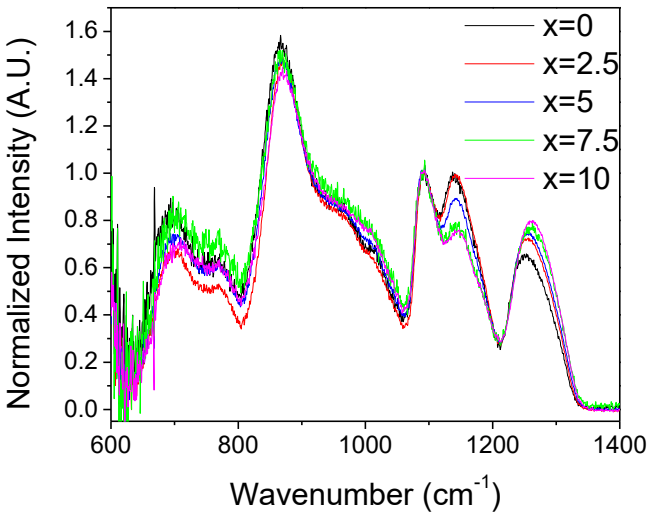

Figure 25. IR spectra of the investigated glasses.

The IR spectra show bands at approximately 880, 1080, 1140 and 1240 cm^{-1}. Several shoulders can also be seen in the range from 980 to 1050 cm^{-1}. In addition, there are broad bands between 650 and 800 cm^{-1}. It should be noted that no bands exist at wavenumbers higher than 1300 cm^{-1}, where the ν(P=O) of Q^3 groups usually appear. This means that no Q^3 groups present in the chosen glass system.

The broad band between 600 and 800 cm^{-1} can be related to symmetric vibrational modes ν_{sym} (P-O-P) of Q^2 units. The bands of 1240, 1140, 880 and ~700 cm^{-1} can be related to the ν_{as}(OPO), ν_{ss}(POP), ν_{as}(POP) and ν_{ss}(POP) fundamental vibrations of Q^2 units, respectively [Ko, 10]. The band at 1080cm^{-1} can be attributed to an overlap between Q^1 units and Q^2 units in metaphosphate. The shoulders at ~980cm^{-1} correspond to the asymmetric stretching vibrations of the PO_3^{2-} in Q^1 units whereas the shoulders at ~950 and at ~1030cm^{-1} have been related to ν_{as}(POP) fundamental vibration of Q^2 units in, small and large rings, respectively [WI, 84].

The increase in x reduces the intensity of most of the bands compared that of the band at 1080cm^{-1} except for the shoulder in the 980-1050cm^{-1} range and for the band at 1240cm^{-1} indicating that the replacement of Na_2O by NaF increases the number of Q^2 units at the expense of Q^1 units. The increase in x also shifts the positions of the bands at 1280, 1160, 880 and ~700 cm^{-1} to higher wavenumbers. As explained in [Cu, 16], this shift in position could be a result of the F-P-F bonds formation when NaF replaces Na_2O. The increase in the intensity of the shoulder at 1010cm^{-1} can reveal an increase in the (PO_3F) bonds as suggested by Murthy et al. [Mu, 63]. The small increase in intensity of the shoulder at 950cm^{-1} with an increase in x could indicate that the long chain structure of the glass is cut to small phosphate rings when the fluorine content in the glasses increases as suggested in [Cu, 16].

The normalized Raman spectra are presented in Figure 26.

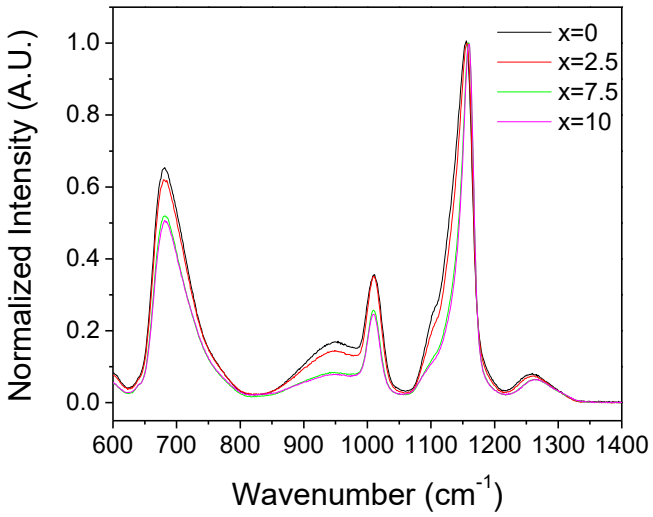

Figure 26. Raman spectra of the investigated glasses.

The spectra exhibit bands at ~700, 800–1050, ~1150 and 1200–1300 cm^{-1}. They are obviously relevant to the metaphosphate structure according to [Me, 97]. There are no typical Q^3 groups' bands at higher than 1300 cm^{-1} as seen in the IR spectra.

The 700-cm^{-1} band corresponds to the symmetric stretching mode of in-chain P-O-P bonds (the bridging oxygen atoms linked with two phosphorous atoms in Q^2 groups) [Ko, 10]. Its intensity is reduced when increasing x, thus showing a decrease in the P-O-P bonds when Na_2O is replaced by NaF. The ~1010-cm^{-1} band can be related to the stretching ν(P-O) of terminal groups (Q^1) [Cu, 16]. When raising x, the intensity of this band decreases indicating that the PO_3F monofluorinated terminal groups continuously replace the P-O bonds in terminal groups. Additionally, the increase in x results in the intensity reduction of the shoulder at ~960-cm^{-1}, attributed to the symmetric PO_4 stretch on Q^0 tetrahedra [Br, 00]. This means that the number of Q^0 units decrease when raising x. An increase in x decreases the intensity of the bands at 1250 and 1100-cm^{-1} attributed to the asymmetric and symmetric stretching of non-bridging ν(PO_2) of Q^2 groups, respectively ([Le, 09], [Ka, 04] and [Ka, 12]). Finally, with increasing x, the position of the band at 1150 cm^{-1} shifts to a higher wavenumber indicating that the metaphosphate chains grow longer, which also showing the rise in Q^2 units at the expense of the Q^1 according to [Cu, 16].

In summary, from the analysis of the IR and Raman spectra of the investigated glasses, the glasses are suspected to have a metaphosphate glasses' network structure. Firstly, the structure contains mainly Q^2 tetrahedra organized in chain and ring type formations. The replacement of Na_2O by NaF leads to the creation of P-F bonds at the expense of P-O bonds increasing the amount of the Q^2 units while decreasing number of the Q^1 ones, meaning that the network connectivity is enhanced when x increases. Combined with the conclusion from the density measurement, the decrease in T_g is supposedly related to the weaker ionic cross-linking of the modifier cations in agreement with [Cu, 16]. Consequently, the reduction in the non-bridging terminal groups and the P-F bonds formation both shift the optical band gap to a lower wavelength when x increases as can be seen from the absorption spectra (Figure 27).

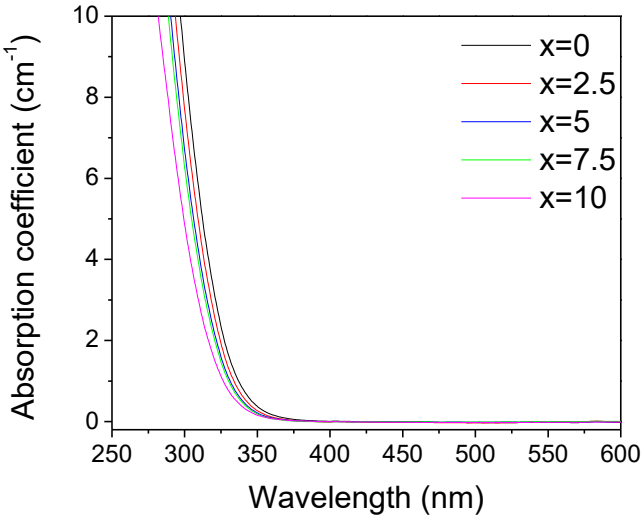

Figure 27. Absorption spectra of several glasses in the system.

4.2 Preparation & characterization of $NaYF_4$-containing glasses

The $NaYF_4$-containing glasses with x=0 and 10 were prepared using direct doping process. First, the process was optimized using persistent luminescent microparticles with the $CaAl_2O_4$: Eu^{2+}, Nd^{3+} composition. Such particles exhibit blue PeL after stopping irradiation.

4.2.1 Optimization of the direct doping process

PeL MPs with the composition $CaAl_2O_4$: Eu^{2+}, Nd^{3+} were used to allow us to optimize the direct doping process. As explained earlier, the doping temperature (T_{doping}) and the dwell time (the "waiting" time before quenching the glass) need to be optimized. Here, 1 weight% of the MPs were added at 3 doping temperatures (575, 600 and 650°C) and the dwell times was varied between 3 and 10 minutes prior to casting. Figure 28 shows the glasses after stopping the UV irradiation.

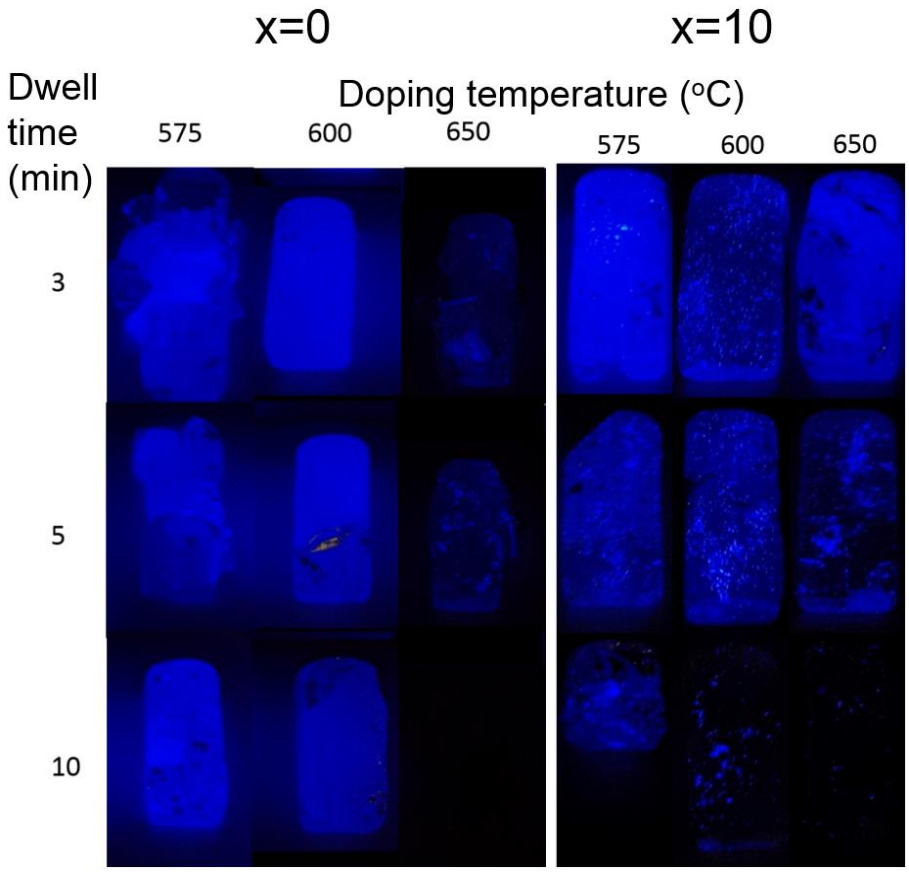

Figure 28. x=0 and x=10 samples after stopping UV irradiation.

All the samples exhibit blue-color persistent luminescence (from the Eu^{2+} ion) after stopping the UV excitation confirming that the MPs survived in the glass matrix. One can notice that the intensity of the blue luminescence from the x=10 glasses is lighter than that of the x=0 glasses when prepared using the same doping temperature and dwell time. It should be pointed out that the x=0 glasses prepared using low doping temperature and short dwell time broke into pieces during the annealing suggesting that a large number of MPs survive in the glass. Aggregates of MPs can be clearly seen in the glasses. This gives us a hint that different glass compositions react differently with the MPs.

To quantify the MPs dispersion, the pictures of the glasses were analyzed using a Java-based image processing software, ImageJ. The software can measure several parameters such as min/max pixel intensity and the corresponding standard deviation (StdDev). Here, we consider that a glass with a low StdDev is a glass with a uniform luminescence and so a uniform dispersion of the MPs in the glass. However, a low StdDev can also be related to the corrosion of the MPs and so to a loss in the PeL properties. Therefore, it is crucial to compare the picture of the glasses to the StdDev to understand clearly the impact of the doping parameters (T_{doping} and dwell time) on the dispersion and survival of the particles in the glass. The StdDev values of pixel intensity obtained from the Figure 28 are displayed in Table 3.

Table 3. Sample codes of x=0 and x=10 as well as their standard deviation of pixel intensity obtained from ImageJ.

T_{doping}(°C)–Dwell time (min)	**StdDev x=0**	**StdDev x=10**
575-3	15	**7**
575-5	10	**9**
575-10	6	15
600-3	**3**	12
600-5	**3**	15
600-10	6	11
650-3	8	9
650-5	8	15
650-10	2	5

One can notice that the StdDev increases when the doping temperature and dwell time increases. However, for high doping temperature, the StdDev decreases due the light PeL from the glasses which can be related to the corrosion of the MPs. For the glasses with x=0, the lowest StdDev was recorded for the glass prepared using 600-5. However, as the glasses prepared using a T_{doping} at 575°C broke, we suspect based on the afterglow picture of the glasses that the dispersion of the MPs in these glasses to be similar than in the glasses prepared using a T_{doping} at 600°C. Similar results were obtained for the glasses with x=10: the most well-dispersed, high-intensity glass was x10-575-3.

The persistent luminescence (PeL) measurement was carried out with crushed powder of the bottom half of each sample. The PeL spectra are shown in Figure 29.

x=0

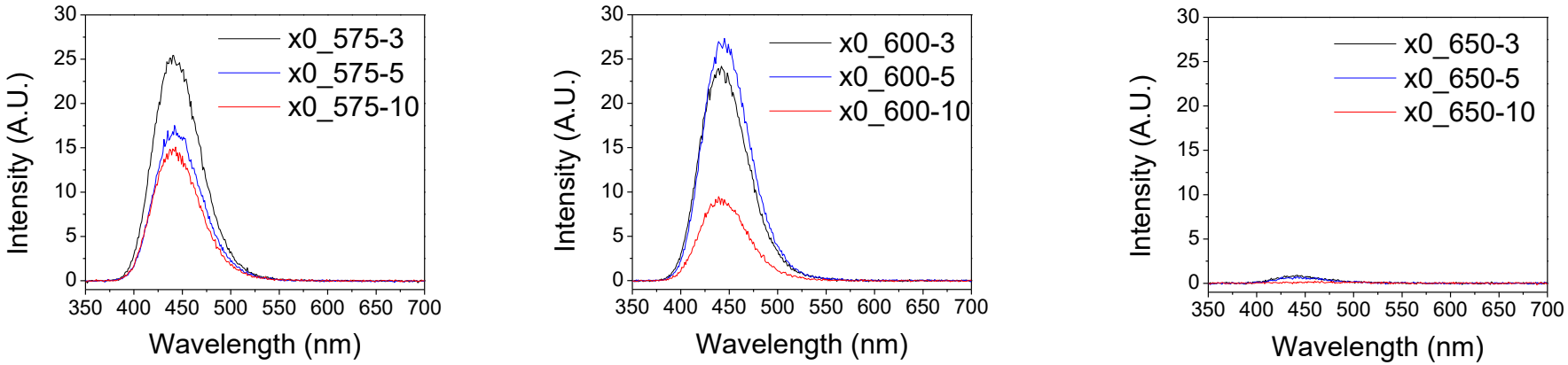

x=10

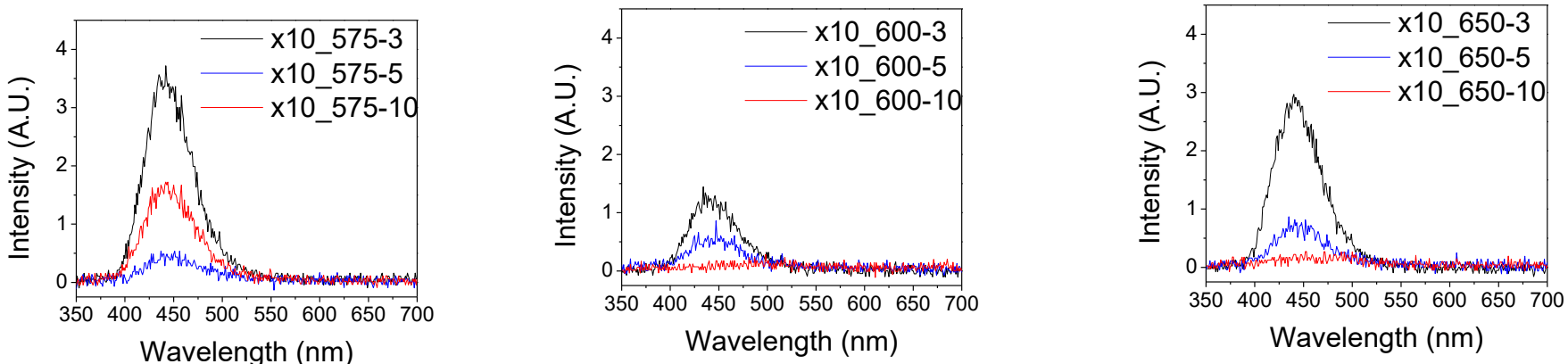

Figure 29. PeL spectra of x=0 and x=10 samples.

The spectra exhibit a single broad band peaking at 445 nm which is ascribed to the $4f^6 5d^1 \rightarrow 4f^7$ transition of the Eu^{2+} ion situated at one Ca^{2+} site in the $CaAl_2O_4$ structure [Av, 12], [Hö, 10]. We confirm that the x=0 glasses exhibit a stronger PeL than the glasses with x=10. As a general comment, the intensity of the emission band decreases as the doping temperature and dwell time increase in agreement with the afterglow picture of the glasses. However, some of the graphs show incoherent results. This must be related to the presence of agglomerates in the glasses. Therefore, we show here that PeL spectra measurement need to be completed with a systematic observation of the glasses after stopping the irradiation.

The conventional luminescence spectra are shown in Figure 30.

x=0

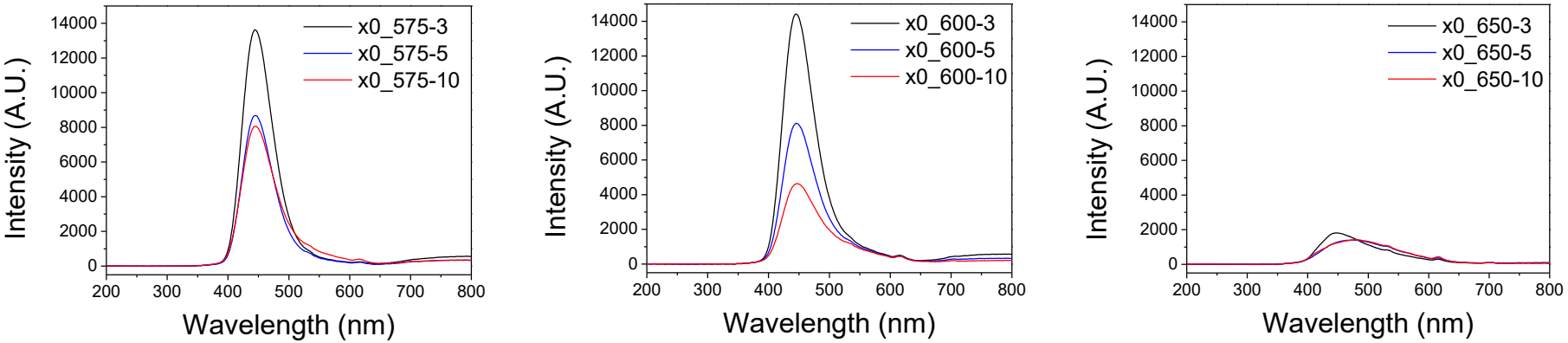

x=10

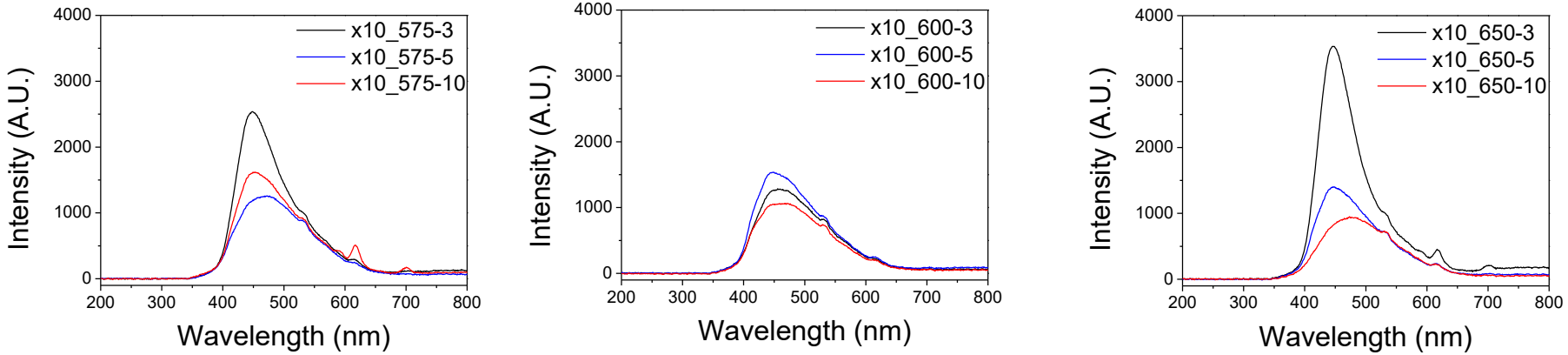

Figure 30. Conventional luminescence of x=0 and x=10 samples.

The spectra exhibit a broad band located at 450 nm which is linked with the emission of Eu^{2+} situated in Ca^{2+} spots [Av, 12]. Additional, the presence of the bands 590, 620 and 700 nm confirms that Eu^{2+} ions oxidize to Eu^{3+} during the glass melting as seen in [Ma, 15].

An increase in the T_{doping} and dwell time leads to a decrease in the PL intensity. We also confirm that the x=0 glasses exhibit stronger PL than the glasses with x=10. As seen with the PeL measurement, incoherent spectra are recorded: the 650-10 glass with x=10 exhibiting larger PL than the 575-3 glass. As explained in the previous paragraph, this is related to the presence of agglomerates in the glasses. It should be pointed out that the emission band related to Eu^{3+} can be seen more in the spectra of the glasses with x=10 indicating that a larger amount of Eu^{2+} are oxidized in the glasses with x=10 than in the glasses with x=0. This is in agreement with the afterglow picture of the glasses.

It should be pointed out that the emission band of the 575-3 glass with x=0 is similar than that of the particles alone whereas the 650-10 glasses with x=0 and 10 and 575-3 glass with x=10 exhibit broader emission band as shown in Figure 31a and b.

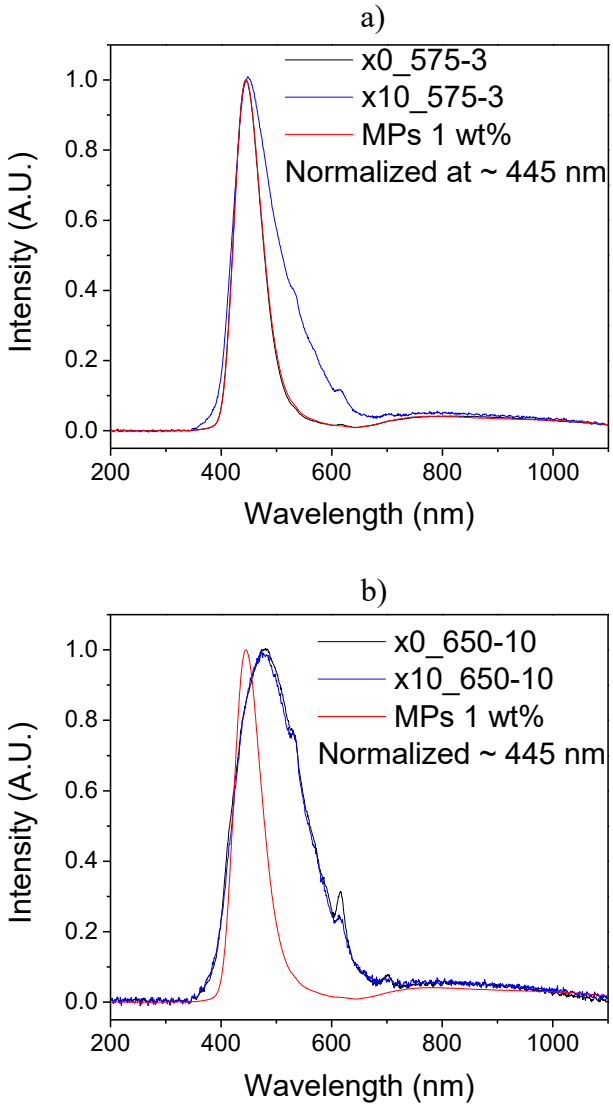

Figure 31. Normalized conventional luminescence of a) 575-3 samples and b) 650-10 samples plus the 1wt% calibration MPs. The excitation wavelength is 266 nm, averaging 10, integration time 50 ms.

Based on Figure 31, the site of the Eu^{2+} ions in the 575-3 glass with x=0 is suspected to be similar than in the MPs alone but different in the other glasses with x=0 and 10.

Figure 32 displays the SEM images for x=0 glasses.

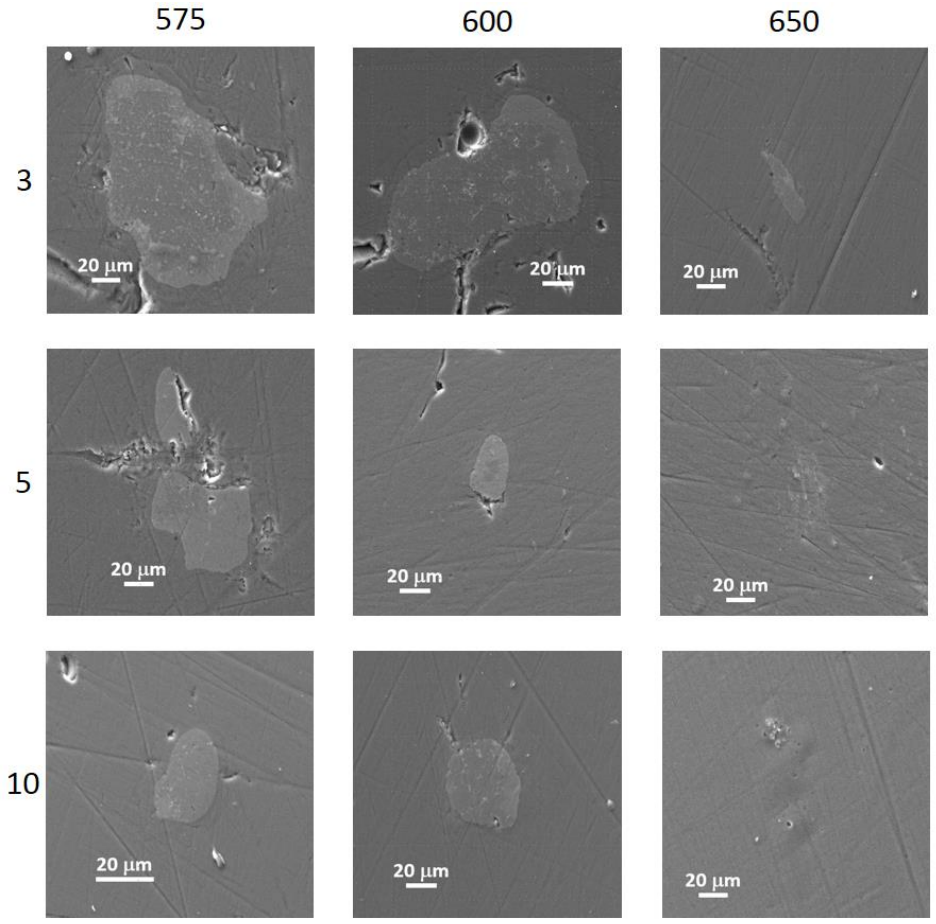

Figure 32. SEM images of particles found in the x=0 glasses.

Generally, the particle size is reduced when increasing the T_{doping} and dwell time. Additionally, there were more changes in the particles themselves—indicating the changes in their integrity. The same was observed for x=10 samples. To investigate further, EDS compositional analysis were utilized. Figure 35 show the EDS line scans of several samples for checking the elements across a microparticle embedded in the glass matrix.

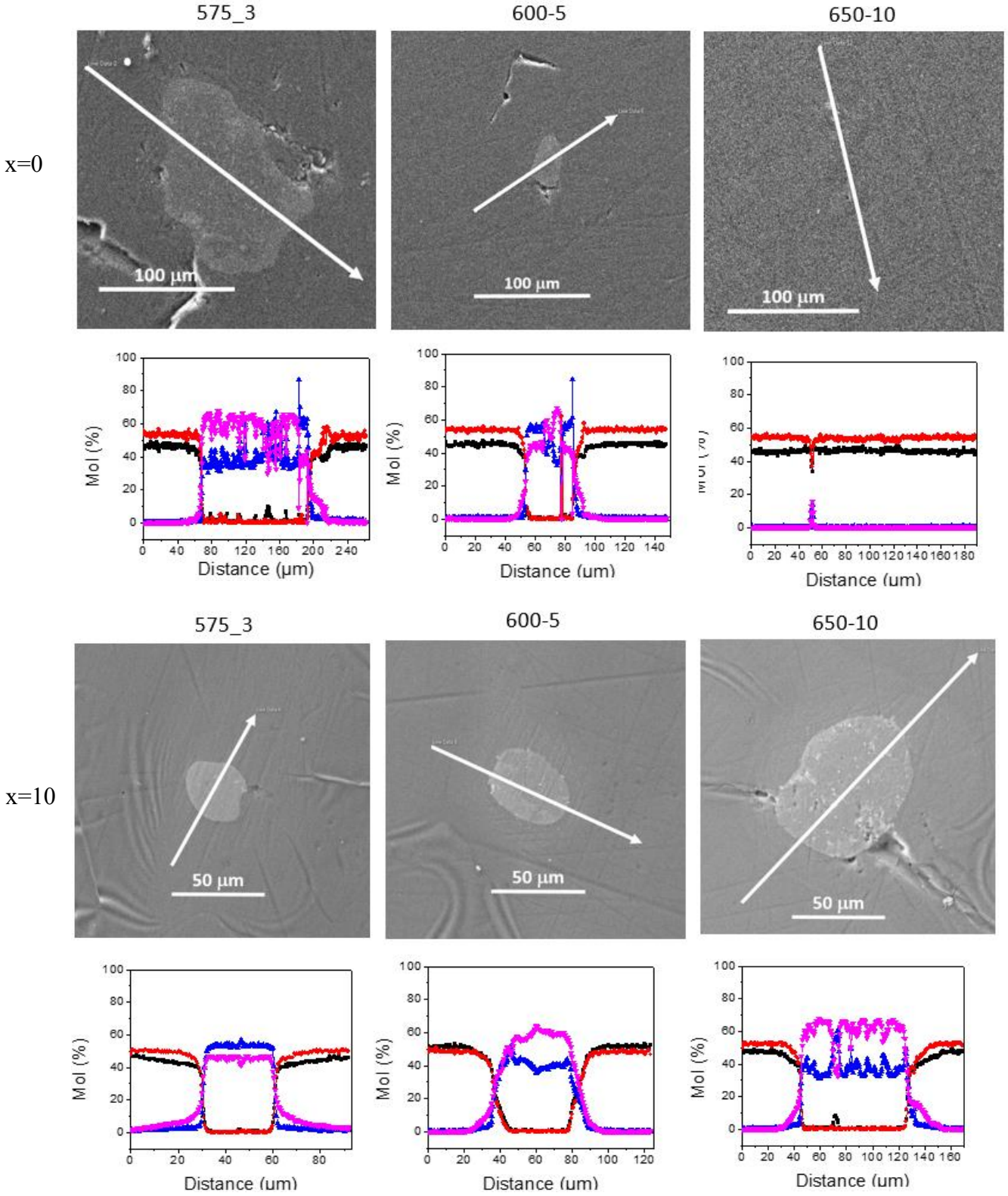

Figure 33. EDS analysis of particles found in x=0 and x=10 glasses doped at different temperatures and dwell times.

For all samples, the glass matrix composition is as targeted within the measurement accuracy (±1.5 mol%). A trace of Al was found in the glasses which can be related to the diffusion of Al from the MPs into the glasses. Based on the composition analysis, the MPs found in the glasses contain only Al_2O_3 and CaO in the center—the MPs generally maintained their composition although the level of integrity varied. Additionally, small amount of Al_2O_3 and CaO are presented around the particles in all samples which is a clear sign of corrosion occurring during the glass preparation. It should be pointed out that the diffusion of the Al and Ca from the MPs into the glass is more visible in the glasses with x=10 than in the glasses with x=0 confirming that corrosion of the MPs occurs more in the glass with x=10 in agreement with the PeL properties of the glasses. Combined with the conventional and persistent luminescence results, the changes in the Eu^{2+} sites probably due to Al, Ca and Eu ions diffusion from the MPs.

In summary, based on the StdDev data and on the PL/PeL properties of the glasses, the particles containing glasses should be prepared using a doping temperature of 575ºC and a dwell time of 3-min to balance the survival and dispersion of the particles in the glass.

4.2.2 $NaYF_4$ nanoparticles-containing glasses

Glasses with x=0 and 10 were prepared by adding 3.75 weight% of $NaYF_4$ nanoparticles synthesized by Dr. Mika Lastusaari from Turku University (Finland). The particles were added in the glass at doping temperature ranging from 575ºC—650ºC and the dwell time was varied from 3 to 5 min as for the preparation of the MPs-containing glasses. As seen in Figure 24, the glass viscosity at the doping temperatures (575, 600 and 650ºC) is below the "5 Pa.s" limit value when doping tellurite glasses as discussed in [Zh, 16]. After being doped, all the glasses are transparent with no visible sign of nanoparticles agglomerates as shown in the Figure 34.

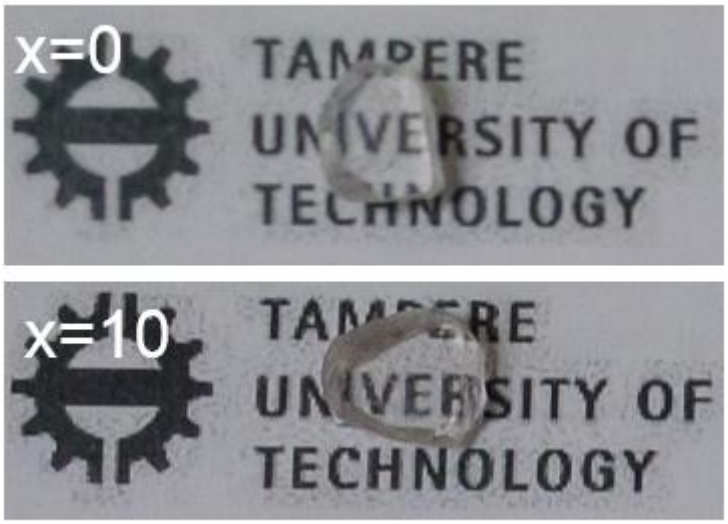

Figure 34. Clear NPs-doped glasses prepared at 575ºC-3min dwell time, taken as examples

The NPs-doped glasses were firstly checked for crystallization. The XRD patterns (not included here) showed no Bragg diffraction from crystalline lattice. This indicates no (or in low amount or too small to be detected) crystals are formed when adding the NPs into the 2 investigated glasses. No change in the glasses' density, thermal and structural properties were observed after adding the NPs due to the low amount of the NPs introduced in the glass networks.

The upconversion of the glasses in the visible was measured using a 974-nm pumping. Upconversion was detected only in the glasses prepared using a doping temperature of 575ºC and a 3-min dwell time confirming the survival of the NPs. Indeed, the concentration of Er_2O_3 and Yb_2O_3 in the glass would be 0.026 mol% and 0.147 mol%, respectively, if the NPs completely dissolve inside the glass during the glass preparation. Therefore, due to the low amount of RE in the glass, no upconversion would be observed if the NPs were completely dissolved in the glass. The Figure 35a shows the upconversion spectra of the glasses.

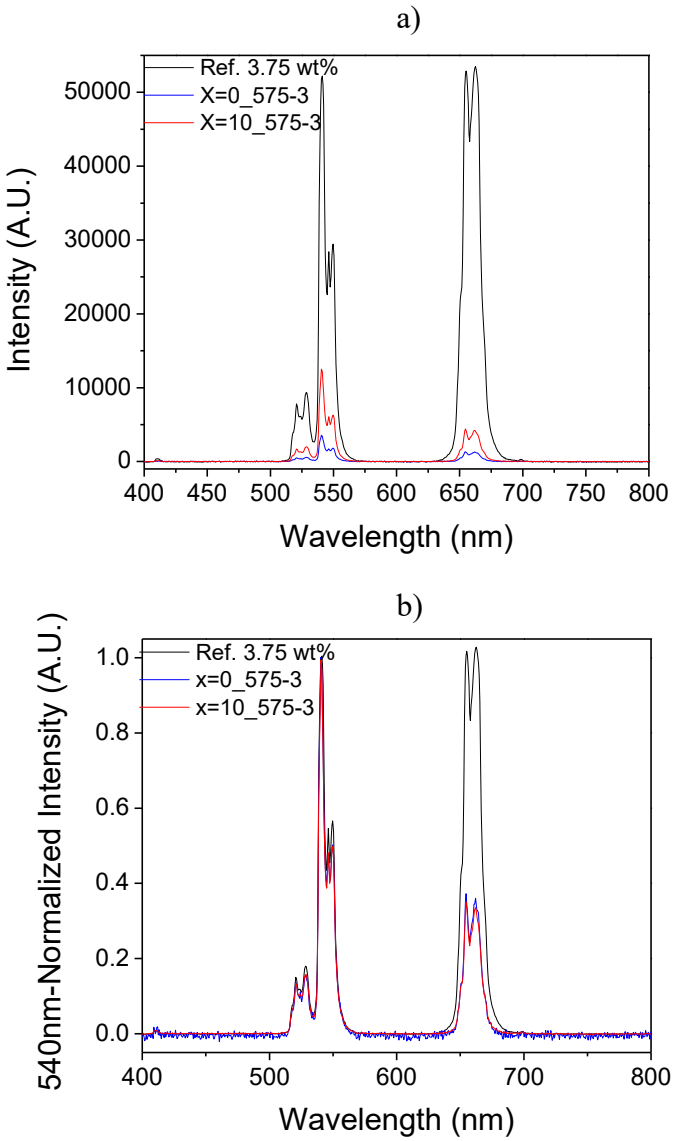

Figure 35. a) Upconversion of 575-3 samples and the reference "calibration" NPs as well as their b) normalized spectra. Upconversion was obtained from 974-nm excitation source, 350-ms integrating time and 100 averages.

Excited by a 974-nm source, the two samples emitted typical emissions of Er^{3+}: green ($^2H_{11/2} - {}^4I_{15/2}$ and $^4S_{3/2} - {}^4I_{15/2}$) and red ($^4F_{9/2} - {}^4I_{15/2}$) light (Figure 35a) [Au, 04]. Surprisingly, the glass with x=10 exhibits stronger upconversion than the glass with x=0. Multiple glasses were prepared using the same direct doping parameters and all the x=10 glasses exhibit strong upconversion compared to the glasses with x=0. Therefore, we think that the corrosion of the NPs occurs less or is slower in the glass with x=10 than in the glass with x=0. As we found that the PeL MPs were more corroded in the glasses with x=10 than in the glasses with x=0, we clearly show that the corrosion of particles in glass melt depends not only on the particles composition but also on the glass batch composition.

Interestingly, one can notice that the spectra clearly display a fine structure—characteristic of Er^{3+} ions coordinated in crystalline sites. In addition, as compared to the upconversion spectra of the NPs alone, small changes in the Stark splitting of Er^{3+} optical transitions can be seen in Figure 35b indicating that embedding the NPs in the glass leads to modifications of the sites of the Er^{3+} ions confirming that corrosion of the NPs with the diffusion of the elements from the NPs in the glass occurs during the glass preparation.

As clear glass is an important requirement for laser application, the transmittance spectra of the glasses were measured. They are presented in Figure 36.

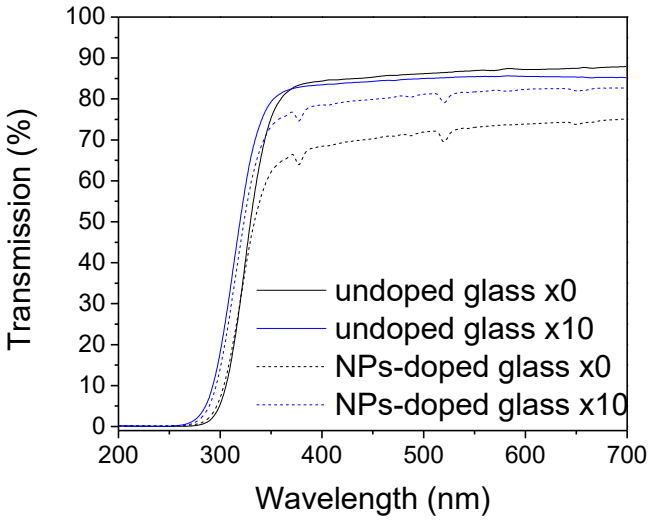

Figure 36. Transmittance of the NPs-free and –containing glasses with x=0 and 10 with a thickness of 3mm [Oj, 17].

The NPs-containing glass with x10 had slightly lower transmittance (approximately 4%) than the NPs-free glass whereas the NPs-containing glass with x=0 exhibits a lower transmittance as compared to the corresponding NPs- free glass. This could be explained by the large amount of bubbles present in the NPs-containing glass with x=0. Therefore, there is an on-going research about the potential relation between the bubbles and the NPs dissolution in the glass.

As mentioned earlier, it is tremendously difficult to directly inspect the embedded NPs in the glass matrix. Only one NPs' agglomerate was found in the NPs-containing glass with x=10 using SEM. Its size was about 250-350µm as seen in Figure 37. The agglomerate contained nanoparticles with the size ranging from 500nm to 1µm. In addition, the EDS analysis detected Yttrium—only presented in the NPs—proving their survival in the glasses as concluded from previous measurements.

a) b)

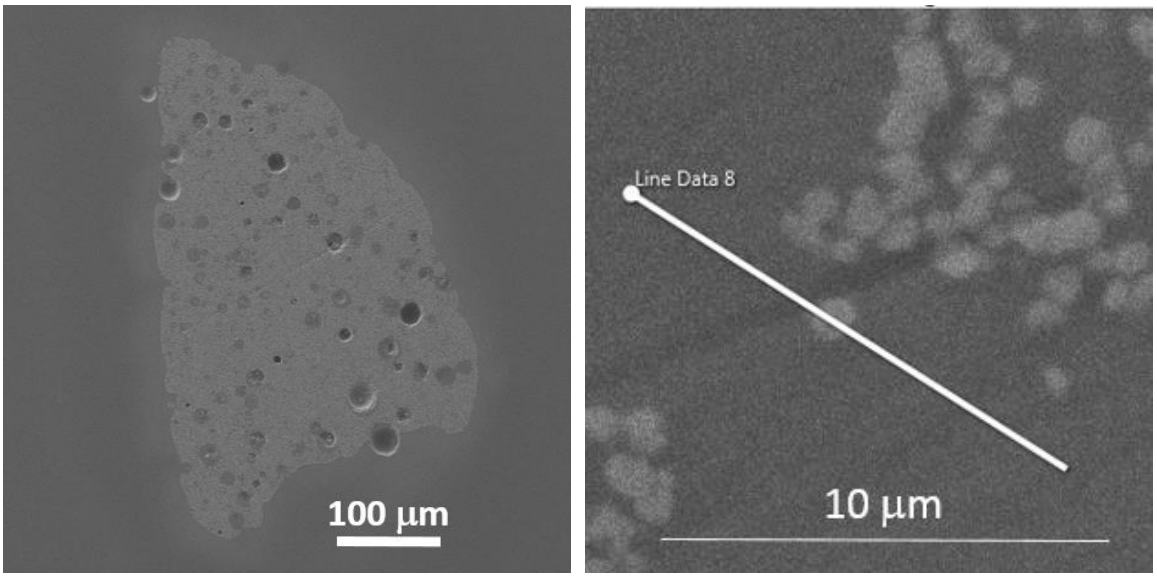

Figure 37. a) A NPs agglomerate embedded in the x=10 glass. b) Nanoparticles having the size of 500nm–1µm presented in the agglomerate.

5. CONCLUSIONS

To sum up, new oxyfluoride glasses were produced in the glass system $45P_2O_5$ – $(55\text{-}x)Na_2O$ – xNaF (mol%) and characterized. The thermal properties of the glasses were measured using DSC technique. We found that the addition of NaF at the expense of Na_2O increases the thermal stability of the glass against crystallization. In addition, the new glasses possess lower melting temperature than 750ºC, making them perfect candidates for doping $NaYF_4$ particles. The density data was obtained by the Archimedes' method and indicated no major changes when altering the composition. The glass structure was also investigated from its IR and Raman spectra: The network was metaphosphate composed of chain and ring formations of Q^2 tetrahedra. It was found that the progressive replacement of Na_2O by NaF led to an increase in the network connectivity.

The direct doping method was applied successfully to fabricate glasses with uniform persistent luminescence when adding $CaAl_2O_4$: Eu^{2+}, Nd^{3+} or upconversion when adding $NaYF_4$: Yb^{3+}, Er^{3+}. The method was first optimized using MPs $CaAl_2O_4$: Eu^{2+}, Nd^{3+} which exhibit blue persistent luminescence after stopping UV irradiation. Three doping temperatures (575, 600 and 650ºC) and dwell times (3, 5 and 10 minutes) were tested in order to balance the survival and dispersion of the particles in the glass. All glasses exhibit blue PeL confirming the survival of MPs. The level of particle distribution was quantified using ImageJ, a Java-based image analysis program, based on pixel intensity. Then, the glass samples crushed to powder for PeL and conventional luminescence (PL) measurement. Finally, the MPs compositional integrity was checked by SEM and EDS analysis. In this experiment, the elements' diffusion from the particles was found to occur already at the T_{doping} of 575ºC and 3-min dwell time. The diffusion of the elements from the MPs into the glasses creates changes in the Eu^{2+} ion sites and leads also to the oxidation of Eu^{2+} to Eu^{3+}.

The upconverter glasses were prepared using directly doping method by adding $NaYF_4$: Yb^{3+}, Er^{3+} nanoparticles. Upconversion in the visible light from the glasses prepared using T_{doping} of 575ºC and 3-min dwell time were observed under a 974-nm excitation source. Indeed, all the 575-3 glasses (regardless of the fluorine content) exhibited strong upconversion in fine-structure spectra, effectively proving the present of remaining NPs in crystalline sites. Also, there was an attempt to locate the embedded NPs using SEM and EDS. One NPs agglomerate was found in the glass with x=10 and clearly possessed Yttrium, confirming the survival of the NPs. Finally, the transmission spectra of the glasses were measured. We found that the addition of NPs decreases slightly the transmittance of the glasses, probably due to the formation of bubbles which are suspected to occur when the particles are added in the glass melt.

In summary, the higher doping temperature and the longer dwell time, the more corrosion of the particles. In this work, the optimized doping parameters are 575°C and 3-minute dwell time but further adjustments are ongoing. Also, the corrosion behavior of the glass melts on the particles was found to depend not only the temperature but also on the particles and glass melts composition: the MPs $CaAl_2O_4$: Eu^{2+}, Nd^{3+} were corroded more heavily in the glass with x=10, while the NPs $NaYF_4$: Yb^{3+}, Er^{3+} were more corroded in the glass with x=0.

Interestingly, there are several challenging issues and practical ideas for to continue this project. Firstly, most of the glass samples are highly hygroscopic—some of them are extremely sensitive to air moisture even in the laboratory condition. This is probably a consequence from the phosphate network being "too open". This level of moisture sensitivity will limit most of applications from the glass system. Therefore, future studies may involve attempts to stabilize this glass system against moisture absorption, by adding appropriate modifiers to the composition to strengthen the network. Secondly, the doping parameters can be tuned even further. For example, instead of 575-600-650°C, the doping temperatures can be narrowed to 555-565 or 580°C. Thirdly, due to its important effect on the survival of particles, the corrosive behavior between the host glass and the dopants should be systematically and thoroughly investigated. Finally, bubbles were found in the NPs-doped glasses, posing intrinsic research questions: Did they come from the completely dissolved NPs and can they be used to estimate the number of lost NPs? This should be further investigated.

REFERENCES

[ASTM, 02] ASTM, Standard Test Method for Measurement of Viscosity of Glass Between 104 Pa s and 108 Pa s by Viscous Compression of a Solid Right Cylinder, C 1351M-96 (2002).

[ASTM, 03] ASTM, Standard Test Method for Measurement of Viscosity of Glass Between Softening and Annealing Range (Approximately 108 Pa s to Approximately 1013 Pa s) by Beam Bending (Metric), C 1350M-96 (2003).

[Au, 04] F. Auzel, Upconversion and Anti-Stokes Processes with f and d Ions in Solids, Chem. Rev., 104 (2004) 139-173.

[Av, 12] N. Avci, K. Korthout, M.A. Newton, P.F. Smet, D. Poelman, Valence states of europium in $CaAl_2O_4$:Eu phosphors, Opt. Mater. Express 2 (2012) 321–330.

[Ba, 01] D.W. Ball, Theory of Raman Spectroscopy, Spectroscopy 16 no. 11 (2001) 32-34.

[Bl, 94] G. Blasse, B. C. Grabmaier, Luminescent Materials, Springer-Verlag Berlin Heidelberg (1994) 232.

[Br, 00] R. K. Brow, Review: the structure of simple phosphate glasses, Journal of Non-Crystalline Solids, 263 (2000) 1-28.

[Br, 11] H. F. Brito, J. Hassinen, J. Hölsä, H. Jungner, T. Laamanen, M. Lastusaari, M. Malkamäki, J. Niittykoski, P. Novák, L. C. V. Rodrigues, Optical energy storage properties of $Sr_2MgSi_2O_7:Eu^{2+},R^{3+}$ persistent luminescence materials, J. Therm. Anal. Calorim. 105(2) (2011) 657–662.

[Ca, 00] J.H. Campbell, T.I. Suratwala, Nd-doped phosphate glasses for high-energy/high-peak-power lasers, Journal of Non-Crystalline Solids, 263 (2000) 318–341.

[Ca, 14] L. Calvez, 10 - Transparent chalcogenide glass-ceramics, In Chalcogenide Glasses, Woodhead Publishing (2014) 310-330, 331e-342e, 331-343.

[Cu, 16] S. Cui, J. Massera, M. Lastusaari, L. Hupa, L. Petit, Novel oxyfluorophosphate glasses and glass-ceramics, Journal of Non-Crystalline Solids, 445 (2016), 40-44.

[Fa, 03] F. Faupel, W. Frank, M.P Macht, Diffusion in Metallic Glasses and Supercooled melts, Reviews of Modern Physics 75 no. 1 (2003) 237-280.

[Ga, 06] F. Gan, L. Xu, Photonic Glasses, World Scientific Pubishing Co. Pte. Ltd (2006) 447.

[Ga, 08] S. Gaylord, Thermal and Structual Properties of Candidate Moldable Glass Types, All Theses (2008) 396.

[Ga, 82] V.P. Gapontsev, S.M. Matitsin, A.A Isineev, V.B. Kravchenko, Erbium glass lasers and their applications, Optics & Laser Technology 14 no. 4 (1982) 189-196.

[Ge, 17] C. Gestraud, J. Massera, L. Petit, A. Fargues, B. Glorieux, D. Marc, T. Cardinal, L. Hupa, Effect of partial crystallization on the structural and Er^{3+} luminescence properties of phosphate-based glasses, Optical Materials 64 (2017) 230-238.

[Gf, 00] T.H. Gfroerer, Photoluminescence in Analysis of Surfaces and Interfaces, In Encyclopaedia of Analytical Chemistry; Meyers, R. A., Ed.; John Wiley and Sons Ltd.: Chichester (2000) 9209-9231.

[Go, 03] J.I. Goldstein, Scanning electron microscopy and X-ray microanalysis, 3rd ed., Kluwer, New York (NY) (2003) 689.

[Ha, 10] R. Hahn, S. Berger, P. Schmuki, Bright visible luminescence of self-organized ZrO_2 nanotubes, J. Solid State Electrochem. 14(2) (2010) 285–288.

[Ha, 57] E.N. Harvey, A History of luminescence: From the Earliest Times Until 1900, Amer. Phil. Soc., Philadelphia, (1957) 601-669.

[He, 01] M. P. Hehlen, M. L. F Philips, N. J. Cockroft, H. U. Güdel, Encyclopedia of Materials: Science and Technology, Burschow, K. H. J., Ed.; Elsevier Science Ltd.: New York 10 (2001) 9456.

[He, 04] S. Heer, K. Kömpe, H. U. Güdel, M. Haase, Highly efficient multicolour upconversion emission in transparent colloids of lanthanide-doped $NaYF_4$ nanocrystals, Adv. Mater. 16 (2004) 2102–2105.

[He, 12] F. B. Hermi, J. Hölsä, T. Laamanen, M. Lastusaari, M. Malkamäki, L. C. V. Rodrigues, Persistent luminescence mechanisms: human imagination at work, Opt. Mater. Express 2 (2012) 371-381.

[Hö, 03] W. Höland, V. Rheinberger, M. Schweiger, Control of nucleation in glass ceramics, Phil. Trans. R. Soc. Lond. A 361 (2003) 575-589.

[Hö, 10] J. Hölsä, T. Laamanen, M. Lastusaari, M. Malkamäki, E. Welter, D.A. Zajac, Valence and environment of rare earth ions in $CaAl_2O_4:Eu^{2+},R^{3+}$ persistent luminescence materials, Spectrochim. Acta Part B 65 (2010) 301–305.

[Hö, 11] J. Hölsä, M. Lindström, A. Kotlov, T. Laamanen, M. Lastusaari, M. Malkamäki, H. F. Brito, L. C. V. Rodrigues, E. Welter, Yellow Persistent Luminescence of the $Sr_3SiO_5:Eu^{2+},R^{3+}$ Materials, Photo Science Annual Report (2011).

[Ib, 12] S. Ibrahim, M. Abdel-Baki, F. El-Diasty, Zinc borophosphate glasses for infra-red-based optical applications, Optical Engineering 51 no. 9 (2012) 93401.

[Je, 14] N. D. Jespersen, Thermal analysis, In AccessScience, McGraw-Hill Education (2014).

[Ji, 97] S. Jiang, M. J. Myers, D.L. Rhonehouse, S.J. Hamlin, J.D. Myers, U. Griebner, K. Schonnagel, H. Schonnagel, Ytterbium-doped phosphate laser glasses, Proc. SPIE, Solid State Lasers VI 2986 (1997) 10.

[Ji, 98] S. Jiang, M. Myers, N. Peyghambarian, Er^{3+} doped phosphate glasses and lasers, Journal of Non-Crystalline Solids 239 no. 1–3 (1998) 143–148.

[Ka, 04] M.A. Karakassides, A. Saranti, I. Koutselas, Preparation and structural study of binary phosphate glasses with high calcium and/or magnesium content, Journal of Non-Crystalline Solids 347 no. 1 (2004) 69-79.

[Ka, 12] A. G. Kalampounias, Short-time vibrational dynamics of metaphosphate glasses, Journal of Physics and Chemistry of Solids 73 no. 2 (2012) 148-153.

[Ke, 80] C. J. Keattch, R. C. Mackenzie, F. W. Wilburn, E. L. Charlsey, P. G. Laye, M. J. Richardson, Fundamentals and quantitative applications of DTA and DSC, Analytical Proceedings 17(6) (1980) 217-231.

[Kl, 15] D. T. Klier, M. U. Kumke, Upconversion Luminescence Properties of $NaYF_4$: Yb: Er Nanoparticles Codoped with Gd^{3+}, The Journal of Physical Chemistry C 2015 119 (6) (2015) 3363-3373.

[Ko, 10] I. Konidakis, C.-P.E. Varsamis, E.I. Kamitsos, D. Möncke, D. Ehrt, Structure and properties of mixed strontium−manganese metaphosphate glasses, J. Phys. Chem. 114 (2010) 9125–9138.

[La, 06] J. R. Lakowicz, Principles of Fluorescence spectroscopy, Springer US (2006) 954.

[Lai, 16] T. Laihinen, Lanthanide doped $NaYF_4$ up-conversion luminescence materials, University of Turku Doctoral dissertation (2016) 78.

[Le, 07] E. Le Bourhis, Glass: Mechanics and Technology, Wiley-VCH Verlag GmbH & Co. KGaA 1–5 (2007).

[Le, 09] S. Lee, A. Obata, T. Kasuga, Ion release from SrO–CaO–TiO_2–P_2O_5 glasses in Tris buffer solution, J. Ceram. Soc. Jpn. 117 (2009) 935–938.

[Le, 14] T. Lever, P. Haines, J. Rouquerol, et al., ICTAC nomenclature of thermal analysis (IUPAC Recommendations 2014), Pure and Applied Chemistry, 86(4) (2014) 545-553.

[Li, 01] T. Lin, Z. Tang, Z. Zhang, X. Wang, J. Zhang, Preparation of a new long afterglow blue-emitting $Sr_2MgSi_2O_7$-based photoluminescent phosphor, J. Mater. Sci. Lett. 20(16) (2001) 1505–1506.

[Li, 02] Y. Lin, Z. Tang, Z. Zhang, C. W. Nan, Anomalous luminescence in $Sr_4Al_{14}O_{25}$:Eu,Dy phosphors, Appl. Phys. Lett. 81(6) (2002) 996–998.

[Lo, 17] P. Lopez-Iscoa, L. Petit, J. Massera, D. Janner, N.G. Boetti, D. Pugliese, S. Fiorilli, C. Novara, F. Giorgis, D. Milanese, Effect of the addition of Al_2O_3, TiO_2 and ZnO on the thermal, structural and luminescence properties of Er^{3+}-doped phosphate glasses, Journal of Non-Crystalline Solids 460 (2017) 161–168.

[Ma, 09] J. C. Mauro, Y. Yue, A. J. Ellison, P. K. Gupta, D. C. Allan, Viscosity of glass-forming liquids, Proceedings of the National Academy of Sciences 106(47) (2009) 19780-19784.

[Ma, 15] J. Massera, M. Gaussiran, P. Gluchowski, M. Lastusaari, L. Hupa, L. Petit, Processing and characterization of phosphate glasses containing $CaAl_2O_4$:Eu^{2+},Nd^{3+} and $SrAl_2O_4$:Eu^{2+},Dy^{3+} microparticles, Journal of the European Ceramic Society 35 no. 14 (2015) 3863-3871.

[Ma, 16] J. Massera, P. Głuchowski, M. Lastusaari, L.C.V. Rodrigues, L. Petit, J. Hölsä, L. Hupa, M. Hupa, New alternative route for the preparation of phosphate glasses with persistent luminescence properties, Journal of the European Ceramic Society 35 no. 4 (2015) 1255–1261.

[Ma, 96] T. Matsuzawa, Y. Aoki, N. Takeuchi, Y. Murayama, A new long phosphorescent phosphor with high brightness, $SrAl_2O_4$:$Eu^{2+}Dy^{3+}$, J. Electrochem. Soc. 143(8) (1996) 2670–2673.

[Me, 97] K Meyer, Characterization of the structure of binary zinc ultraphosphate glasses by infrared and Raman spectroscopy, Journal of Non-Crystalline Solids 209 no. 3 (1997) 227-239.

[Mu, 63] M.K. Murthy, Phosphate-halide systems: II, infrared spectra of glasses in the system $NaPO_3$–NaF, J. Am. Ceram. Soc. 46 (11) (1963) 558–559.

[Ng, 17] H. Nguyen, M. Tuomisto, J. Oksa, T. Salminen, M. Lastusaari, L. Petit, Upconversion in low rare-earth concentrated phosphate glasses using direct $NaYF_4$:Er^{3+}, Yb^{3+} nanoparticles doping, Scripta Materialia 139 (2017) 130-133.

[Oj, 17] N. Ojha, H. Nguyen, T. Laihinen, T. Salminen, M. Lastusaari, L. Petit, Corrosion of microparticles in phosphate glass melt, Paper submitted to Corrosion Science Journal, Elsevier B.V. (2017), Ref: CORSCI_2017_1335.

[Or, 07] Orton Model PPV-1000 Parallel-Plate Viscometer, Westerville, OH, Edward Orton Jr. Ceramics Foundation (2007).

[Pa, 09] J. d. Paula, P. Atkins, Elements of physical chemistry (5th ed.), Oxford: Oxford U.P. (2009) 459.

[Pa, 14] S. Pau, Photonics, In AccessScience, McGraw-Hill Education (2014).

[Pa, 17] R. Paschotta, Photoluminescence, Encyclopedia of Laser Physics and Technology - photoluminescence, PL spectrum, fluorescence (2017).

[Pe, 05] Perkin Elmer Life and Analytical Sciences, FT-IR Spectroscopy Attenuated Total Reflectance (ATR) (2005).

[Pu, 16] D. Pugliese, N.G. Boetti, J. Lousteau, E. Ceci-Ginistrelli, E. Bertone, F. Geobal-do, D. Milanese, Concentration quenching in an Er-doped phosphate glass for compact optical lasers and amplifiers, Journal of Alloys and Compounds 657 (2016) 678–683.

[Ru, 37] H. Rupp, Die Leuchtmassen und ihre Verwendung - eine Einführung in Fluoreszenz und Phosphoreszenz der festen Körper, Gebr. Bornträger (1937).

[Sc, 92] G. W. Scherer, Editorial Comments on a Paper by Gordon S. Fulcher, Journal of the American Ceramic Society 75 (1992)1060–1062.

[Sh, 05] J.E. Shelby, Introduction to glass science and technology, Royal Society of Chemistry, Cambridge (2005) 308.

[So, 05] J.G. Solé, L.e. Bausá, D. Jaque, Fundamentals, An Introduction to the Optical Spectroscopy of Inorganic Solids, John Wiley & Sons, Ltd (2005) 1–38.

[Ti, 10] B. Tincher, J. Massera, L. Petit, K. Richardson, Viscosity properties of tellurite-based glasses, Materials Research Bulletin 45 no. 12 (2010) 1861-1865.

[Tu, 15] L. Tu, X. Liu, F. Wu, H. Zhang, Excitation energy migration dynamics in upconversion nanomaterials, Chemical Society reviews 44 no. 6 (2015) 1331-1345.

[WI, 84] J. A. WILDER, J. E. SHELBY, Property Variation in Alkali Alkaline-Earth Metaphosphate Glasses, Journal of the American Ceramic Society 67 (1984) 438–444.

[Ya, 00] M. Yamane, Y. Asahara, Glasses for Photonics, Cambridge University Press, Cambridge (2000) 284.

[Ya, 97] H. Yamamoto, T. Matsuzawa, Mechanism of long phosphorescence of $SrAl_2O_4:Eu^{2+},Dy^{3+}$ and $CaAl_2O_4:Eu^{2+},Nd^{3+}$, J. Lumin. 72-74 (1997) 287–289.

[Zh, 16] J. Zhao, X. Zheng, E. P. Schartner, P. Ionescu, R. Zhang, T.-L. Nguyen, D. Jin, H. Ebendorff-Heidepriem, Upconversion Nanocrystal-Doped Glass: A New Paradigm for Photonic Materials, Advanced Optical Materials 4 (2016) 1507–1517.